Modal added-mass matrix of an elongated flexible cylinder immersed in a narrow annular fluid, considering various boundary conditions. New theoretical results and numerical validation

Romain Lagrange, Maria Adela Puscas, Philippe Piteau, Xavier Delaune, Jose Antunes

Modal added-mass matrix of an elongated flexible cylinder immersed in a narrow annular fluid, considering various boundary conditions. New theoretical results and numerical validation

Romain Lagrange[a], Maria Adela Puscas[b], Philippe Piteau[a], Xavier Delaune[a], Jose Antunes[c]

[a] *Université Paris-Saclay, CEA, Service d'Etudes Mécaniques et Thermiques, F-91191, Gif-sur-Yvette, France*
[b] *Université Paris-Saclay, CEA, Service de Thermo-hydraulique et de Mécanique des Fluides, F-91191, Gif-sur-Yvette, France*
[c] *Centro de Ciências e Tecnologias Nucleares, Instituto Superior Técnico, Universidade de Lisboa, Estrada Nacional 10, Km 139.7, 2695-066 Bobadela LRS, Portugal*

Abstract

This paper considers the fluid-structure interaction problem of two coaxial cylinders separated by a thin layer of fluid. The flexible inner cylinder is imposed a small amplitude harmonic displacement corresponding to a dry vibration mode of an Euler-Bernoulli beam, while the external cylinder is rigid. A new theoretical formulation based on the assumption of a narrow fluid annulus is derived to estimate the modal added-mass matrix of the vibrating cylinder. This formulation accounts for the finite length of the flexible cylinder, clearly highlights the effect of the aspect ratio of the vibrating cylinder on the structure of the added-mass matrix, and covers all types of classical boundary conditions in the same theory and can easily be implemented in any numerical computing environment. The diagonal coefficients of the added-mass matrix are shown to increase with the confinement, with the aspect ratio of the flexible cylinder, and are sensitive to the wave-number of the vibration mode. Also importantly, we show that the dry vibration modes generate off-diagonal coefficients that vanish for an infinitely long cylinder. Our theoretical observations are corroborated by an extensive set of CFD numerical simulations, covering all types of classical boundary conditions, different confinement configurations, and different aspect ratios of the vibrating cylinder. The results obtained are presented in graphical form, which can be directly applied in engineering applications.

Keywords: Vibration modes; Fluid-Structure Interaction; Modal added-mass; Finite length coaxial cylinders, Narrow annulus

1. Introduction

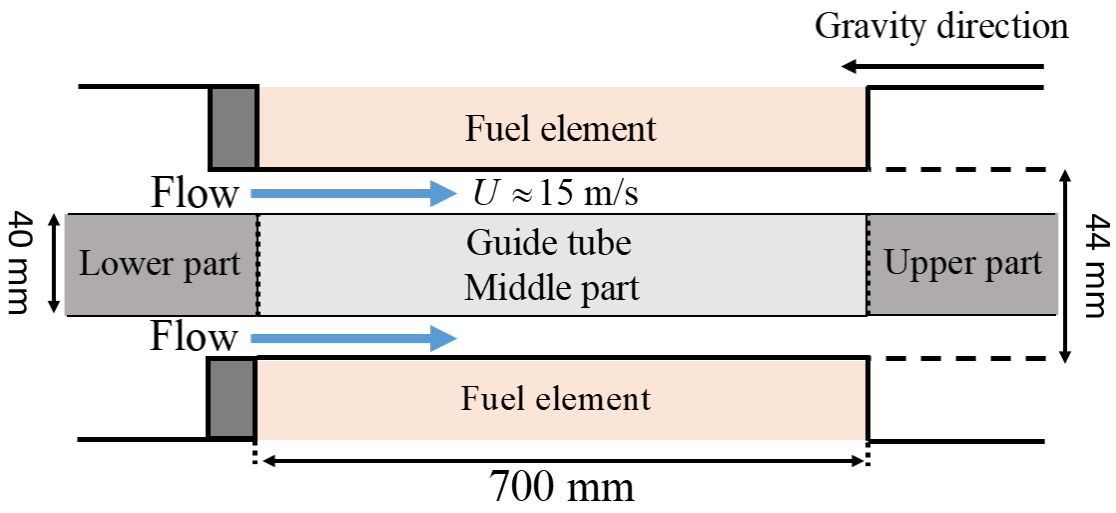

Figure 1: Schematic diagram of a guide tube used in the Jules Horowitz Reactor.

Email addresses: romain.lagrange@cea.fr (Romain Lagrange), romain.g.lagrange@gmail.com (Romain Lagrange)

This study is motivated by the need for a theoretical model to predict the vibrations of guide tubes used in the Jules Horowitz reactor. This test reactor, localized at Cadarache in France, is mainly dedicated to researching materials and fuels for the nuclear power industry and nuclear medicine, see [1] for more details. The reactor core is made of cylindrical fuel elements of length $L = 0.7$ m, see Fig. 1. Aluminum flexible cylindrical guide tubes, of length 2.1 m and outer diameter $2R_1 = 40$ mm, are inserted in the free space between fuel elements to guide experimental devices to be tested. The diameter of this free space is $2R_2 = 44$ mm so that the middle part of the guide tubes is strongly confined (2 mm clearance). As the fuel elements, this part is subject to an axial flow from the primary circuit, with a characteristic speed of the order of 15 m/s. A classical approach to model the dynamics of a flexible structure subject to an axial flow is to expand its displacement on a set of orthogonal vibration modes. The dynamics of the modal amplitudes are governed by a linear-damped oscillator equation, with a forcing term corresponding to the reaction of the fluid. In general, the fluid reaction can be expressed as a linear combination of the acceleration, velocity, and displacement of the immersed structure. The coefficients of this linear combination are the so-called modal added-mass, damping, and stiffness coefficients, respectively. The added-mass is the inertia of the entrained fluid, see [2]. It can be imaged as a virtual mass added to the structure resulting from the acceleration of the surrounding fluid. Similarly, the added damping can be imaged as a virtual dissipation force resulting from the viscous effects of the fluid. The added-stiffness encompasses the part of the fluid force that is in phase with the displacement of the structure and that depends on the velocity of the axial flow, contrarily to the added-mass coefficient. The prediction of the added coefficients is necessary to analyze the dynamic response of the submerged structure in the most suitable manner. In general, these coefficients are functions of the geometry of the immersed body, the shape of the vibration modes, and the degree of confinement of the fluid, see [3, 4, 5, 6, 7, 8, 9]. The modal added-mass can be extracted from the fluid force acting on the flexible structure when immersed in a fluid at rest and imposed a vibration mode. In the case of an elongated flexible body subject to an axial flow, a usual approach to extract the modal added-mass coefficients is to consider the body as a slender structure made of rigid cross sections, see [10, 11, 12, 13, 2, 14, 15]. In such a case, the modal added-mass coefficients can be obtained from a two-dimensional potential-flow theory, see [12, 13]. Given its simplicity, the slender-body theory is handy for estimating the modal added-mass coefficients. Still, it is irrelevant in the context of the Jules Horowitz reactor, as the guide tubes are not slender enough, i.e., $L/R_1 = 35$.

This paper reconsiders the analytical calculation of the modal added-mass coefficients of an elongated, but finite length, flexible cylinder vibrating in a narrow coaxial cylindrical duct. This problem can be solved in the framework of a three-dimensional potential-flow theory, as done in [16]. However, this approach is not flexible enough to be used in an engineering environment as it involves Bessel functions and generalized force Fourier-transform method, leading to a non-closed form solution for the added-mass matrix. Also, it does not explicit the effect of the aspect ratio and the boundary conditions of the flexible cylinder. As these boundary conditions are not properly identified in the Jules Horowitz project, a parametric study that covers different types of classical boundary conditions is needed. Consequently, in the present study, we carry out an inviscid theory and use the simplifying assumption of a narrow annulus, see [17, 18], to provide a more tractable method that yields a new analytical formulation of the modal added-mass coefficients, presenting a number of advantages:

— this formulation does not rely on the slender-body approximation so that it applies to elongated cylinders with finite aspect ratios, as is the case in the Jules Horowitz reactor project,
— this formulation clearly highlights the effect of the aspect ratio on the structure (existence of off-diagonal terms, symmetry, sign, and variations of the coefficients) of the modal added-mass matrix,
— this formulation covers in a single theory all types of classical boundary conditions of the flexible inner cylinder,
— this formulation is fully dimensionless so that it can be used in confined configurations that are not explicitly studied in the present manuscript, as long as the assumption of a narrow gap is fulfilled.

The paper is organized as follows. The presentation of the problem and the governing equations are introduced in § 2. In § 3, we briefly describe the numerical CFD tools used to corroborate the theoretical predictions. In § 4, we discuss why it is necessary to account for the finite length of the vibrating cylinder to predict the added-mass coefficients correctly. In § 5, Appendix B, Appendix E, and Appendix F, we present a new theoretical formulation to estimate the modal added-mass matrix of the vibrating cylinder. Appendix D and Appendix C provide a comparison of the new theoretical formulation with those of [18] and [19]. A comparison between theoretical predictions and numerical results is presented in § 6, Appendix H, and Appendix G, considering all the boundary conditions listed in Appendix A. In § 7, we discuss the relative deviation between theoretical and numerical predictions. Finally, some conclusions are drawn in § 8, which highlight the relevance of the proposed analysis and the practical significance of the results obtained.

2. Definition of the problem and governing equations

2.1. Dimensional equations

We consider the three-dimensional problem of two coaxial cylinders (axes along $\mathbf{e}_x$) separated by a thin layer of fluid. The inner cylinder $\mathcal{C}_1$ is flexible and points on its lateral boundary are imposed a simple harmonic displacement $\Re\left\{\mathrm{e}^{\mathrm{i}\Omega T}\mathbf{Q}_i\left(X,Y\right)\right\}$ with Ω the angular frequency, T the dimensional time, X the longitudinal coordinate, Y the transverse coordinate, $\Re$ the real part operator and i the imaginary complex unit. The displacement profile is of the form

$$\mathbf{Q}_i(X,Y) = Q_i(X)\mathbf{e}_y + \Theta_i(X,Y)\mathbf{e}_x, \tag{1}$$

with

$$Q_i\left(X\right) = Q\,\frac{W_i\left(X\right)}{N_i}, \quad \Theta_i(X,Y) = -Y\frac{dQ_i}{dX}(X), \tag{2}$$

the displacement of the neutral axis and the displacement due to the rotation of the cross-sections, respectively. The rotational displacement Θ_i is set so that the cross-sections remain orthogonal to the cross axis. In equation (2), Q is the amplitude of the displacement, $W_i(X)$ is the i-th bending dry mode of vibration of an Euler-Bernoulli beam and $N_i = \sup\left(|W_i\left(X\right)|, X\in[0,L]\right)$ its infinite norm. The external cylinder $\mathcal{C}_2$ is rigid and fixed. The cylinders radii are R_1 and R_2, boundaries ∂C_1 and ∂C_2 with outward unit normal vectors $\mathbf{n}_1$ and $\mathbf{n}_2$, respectively. The inner cylinder has a length L while the external cylinder is supposed to be infinitely long, as illustrated in Fig.2. The fluid is Newtonian, homogeneous, of volume mass density ρ and dynamic viscosity ν. The Navier-Stokes equations and the boundary conditions for the incompressible fluid flow $\Re\left\{\mathrm{e}^{\mathrm{i}\Omega T}(\mathbf{V}_i,P_i)\right\}$ generated by the displacement $\mathbf{Q}_i$ write

$$\nabla\cdot\mathbf{V}_i = 0, \tag{3a}$$

$$\mathrm{i}\Omega\mathbf{V}_i + \left(\Re\left\{\mathrm{e}^{\mathrm{i}\Omega T}\mathbf{V}_i\right\}\cdot\nabla\right)\mathbf{V}_i + \frac{1}{\rho}\nabla P_i - \nu\Delta\mathbf{V}_i = \mathbf{0}, \tag{3b}$$

$$\mathbf{V}_i - \mathrm{i}\Omega\mathbf{Q}_i = \mathbf{0} \quad \text{on } \partial C_1, \tag{3c}$$

$$\mathbf{V}_i = \mathbf{0} \quad \text{on } \partial C_2, \tag{3d}$$

$$P_i = 0 \quad \text{at } X=0 \text{ and } X=L. \tag{3e}$$

The third equation expresses the continuity of velocities at the boundary of the inner cylinder. The choice for the pressure boundary conditions at $X=0$ and $X=L$ is dictated by the fact that the lower and upper parts of the guide tubes used in the Jules Horowitz reactor are immersed in large volumes of fluid (only the middle part of the guide tubes is confined), see Fig. 1. The linear fluid force $\Re\left\{\mathrm{e}^{\mathrm{i}\Omega T}\mathbf{F}_i\left(X\right)\right\}$ acting on $\mathcal{C}_1$ is given by the integral of the pressure field and the viscous stress tensor on the orthoradial contour $\partial^\Gamma C_1$ of ∂C_1. This writes

$$\mathbf{F}_i = -\int\limits_{\partial^\Gamma C_1} P_i\mathbf{n}_1 d\Gamma + \rho\nu\int\limits_{\partial^\Gamma C_1}\left[\nabla\mathbf{V}_i + (\nabla\mathbf{V}_i)^{\mathrm{T}}\right]\cdot\mathbf{n}_1 d\Gamma, \tag{4}$$

with $d\Gamma$ an infinitesimal line element of integration and T the transpose operator. The modal added-mass coefficient M_{ij} is defined as the projection of the fluid force component $\mathbf{F}_i\cdot\mathbf{e_y}$ generated by the i-th normalized mode W_i/N_i onto the j-th normalized mode W_j/N_j

$$M_{ij} = \frac{1}{N_j}\Re\left\{\frac{\langle\mathbf{F}_i\cdot\mathbf{e}_y, W_j\rangle}{Q\Omega^2}\right\}, \tag{5}$$

with $\langle F,G\rangle = \int_0^L F(X)G(X)dX$.

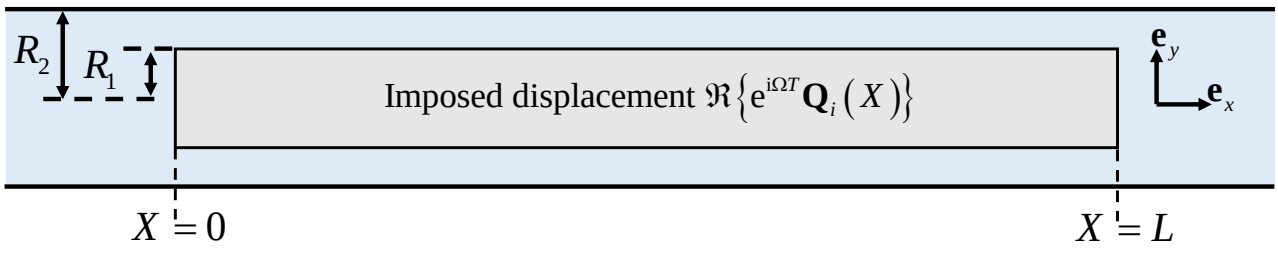

Figure 2: Schematic diagram of two coaxial cylinders separated by a thin layer of fluid. The inner cylinder is imposed a small amplitude harmonic oscillation which generates an incompressible fluid flow.

2.2. Dimensionless equations

Introducing $x = X/L$ and $t = T\Omega$ as the dimensionless axial coordinate and time, we define the dimensionless fluid flow $(\mathbf{v}_i, p_i)$ and linear fluid force $\mathbf{f}_i$ as

$$\mathbf{V}_i = Q\Omega\, \mathbf{v}_i, \quad P_i = \rho Q R_1 \Omega^2\, p_i, \quad \mathbf{F}_i = \rho Q \left(R_1\Omega\right)^2 \mathbf{f}_i. \tag{6}$$

The dimensionless displacement is $\mathbf{q}_i = \mathbf{Q}_i/Q = w_i/N_i\mathbf{e}_y + \theta_i/N_i\mathbf{e}_x$ with $w_i(x) = W_i(Lx)$ the i-th vibration mode expressed in term of the dimensionless longitudinal coordinate x. The dimensionless rotational displacement is $\theta_i(x,y) = -R_1/L\; y\; dw_i/dx$, with $y = Y/R_1$ the dimensionless transverse coordinate. The dimensionless added-mass coefficient m_{ij} is defined as $m_{ij} = M_{ij}/\left(\rho\pi R_1^2 L\right)$, which from equation (5) writes

$$m_{ij} = \frac{1}{N_j}\frac{1}{\pi}\Re\left\{\langle \mathbf{f}_i \cdot \mathbf{e}_y, w_j\rangle\right\}, \tag{7}$$

with $\langle f, g\rangle = \int_0^1 f(x)g(x)dx$. To reduce the number of parameters of the problem we also introduce the rescaled quantities

$$l = \frac{L}{R_1}, \quad \varepsilon = \frac{R_2}{R_1}, \quad KC = \frac{Q}{R_1}, \quad Sk = \frac{\Omega R_1^2}{\nu}, \tag{8}$$

as the aspect ratio, the radius ratio, the Keulegan-Carpenter number and the Stokes number, respectively. Introducing equation (6) in equation (3), the dimensionless Navier-Stokes equations write

$$\nabla^* \cdot \mathbf{v}_i = 0, \tag{9a}$$

$$\mathrm{i}\mathbf{v}_i + \frac{KC}{\varepsilon - 1}\left(\Re\left\{\mathrm{e}^{\mathrm{i}t}\mathbf{v}_i\right\}\cdot\nabla^*\right)\mathbf{v}_i + \frac{1}{\varepsilon-1}\nabla^* p_i - \frac{1}{Sk}\left(\frac{1}{\varepsilon-1}\right)^2\Delta^*\mathbf{v}_i = \mathbf{0}, \tag{9b}$$

$$\mathbf{v}_i - \mathrm{i}\mathbf{q}_i = \mathbf{0} \quad \text{on } \partial C_1, \tag{9c}$$

$$\mathbf{v}_i = \mathbf{0} \quad \text{on } \partial C_2, \tag{9d}$$

$$p_i = 0 \quad \text{at } x = 0 \text{ and } x = 1, \tag{9e}$$

with $\nabla^* = (R_2 - R_1)\nabla$ and $\Delta^* = (R_2 - R_1)^2\Delta$ the dimensionless differential operators. From equation (9b) it clearly appears that the nonlinear term of the Navier-Stokes equations scales as $KC/(\varepsilon - 1)$, so that it increases with the amplitude of the imposed displacement and with the confinement. The viscous term, which scales $Sk^{-1}(\varepsilon-1)^{-2}$, decreases with the forcing frequency and increases with the confinement. In our numerical simulations, the amplitude and the frequency of the imposed displacement will be set to minimize both nonlinear and viscous effects.

3. Numerical simulations

The numerical simulations of the Navier-Stokes equations are performed with the open-source code TrioCFD, a Computational Fluid Dynamics code for incompressible or quasi-incompressible fluids. In what follows, we give a brief description of this code and refer the reader to [20] for specific details.

3.1. The Arbitrary Lagrange-Eulerian method

In TrioCFD, a fluid-structure interaction problem involving moving boundaries is solved using an Arbitrary Lagrange-Eulerian method (ALE). A fluid particle is identified by its position relative to a frame moving with a nonuniform velocity $\mathbf{v}_{i,ALE}$, and in which the dimensionless Navier-Stokes equations (9a) and (9b) write

$$\nabla^* \cdot \mathbf{v}_i = 0, \tag{10a}$$

$$\mathrm{i}\mathbf{v}_i + \frac{KC}{\varepsilon-1}\left(\Re\left\{\mathrm{e}^{\mathrm{i}t}\mathbf{v}_i\right\}\cdot\nabla^*\right)\mathbf{v}_i - \frac{KC}{\varepsilon-1}\left(\Re\left\{\mathrm{e}^{\mathrm{i}t}\mathbf{v}_i\right\}\cdot\nabla^*\right)\mathbf{v}_{i,ALE} + \frac{1}{\varepsilon-1}\nabla^* p_i - \frac{1}{Sk}\left(\frac{1}{\varepsilon-1}\right)^2\Delta^*\mathbf{v}_i = \mathbf{0}. \tag{10b}$$

The ALE method is a hybrid description between the Euler and the Lagrange descriptions of motion, both of them corresponding to the particular cases $\mathbf{v}_{i,ALE} = \mathbf{0}$ and $\mathbf{v}_{i,ALE} = \mathbf{v}_i$, respectively. In the ALE framework, the choice of $\mathbf{v}_{i,ALE}$ is arbitrary as long as the deformation of the mesh grid remains under control. For moderate deformations, $\mathbf{v}_{i,ALE}$ is usually defined as the solution of an auxiliary Laplace problem

$$\Delta^*\mathbf{v}_{i,ALE} = \mathbf{0}, \tag{11a}$$

$$\mathbf{v}_{i,ALE} - \mathrm{i}\mathbf{q}_i = \mathbf{0} \quad \text{on } \partial C_1, \tag{11b}$$

$$\mathbf{v}_{i,ALE} = \mathbf{0} \quad \text{on } \partial C_2, \tag{11c}$$

from which the kinematics of the mesh grid is updated.

3.2. Solving the Navier-Stokes equations

In our simulations, a first order backward Euler scheme is used to discretize the Navier-Stokes equations (10), leading to

$$[D]{\mathbf{v}_i}^{n+1} = \mathbf{0}, \quad (12a)$$

$$[M]\left(J^{n+1}{\mathbf{v}_i}^{n+1} - J^n{\mathbf{v}_i}^n\right) - J^{n+1}\left([A]{\mathbf{v}_i}^{n+1} - [L({\mathbf{v}_i}^n)]{\mathbf{v}_i}^{n+1} + [L({\mathbf{v}_i}^n)]{\mathbf{v}_{i,ALE}}^{n+1} - [G]{p_i}^{n+1}\right) = \mathbf{0}. \quad (12b)$$

In equation (12), J is the Jacobian of the transformation between the ALE and the Lagrange descriptions, $[D]$, $[M]$, $[A]$, $[L(\mathbf{v}_i)]$ and $[G]$ are the discrete divergence, mass, diffusion, nonlinear and gradient matrix operators, respectively. The numerical approach to compute these discrete operators is based on the hybrid Finite Element-Volume method [20, 21] for tetrahedral grids. The discrete pressure is defined on the primal mesh grid, while the discrete velocity is defined on a face-based staggered dual grid. As in Finite Volume approaches, the local equations are integrated over control volumes. The mass equation (12a) is integrated over the primal mesh cells, whereas the momentum equation (12b) is integrated over the dual mesh cells. A dual control volume is obtained by joining the barycenters G_i and G_j of two adjacent triangular cells K_i and K_j, respectively, see Fig. 3 (a). The fluxes and the differential operators are computed employing a Finite Element formulation.
In our simulations, the velocity is computed at the cell faces, and the pressure is computed at the element barycenters and the element nodes, see Fig. 3 (b). A second order upwind MUSCL scheme (Monotonic

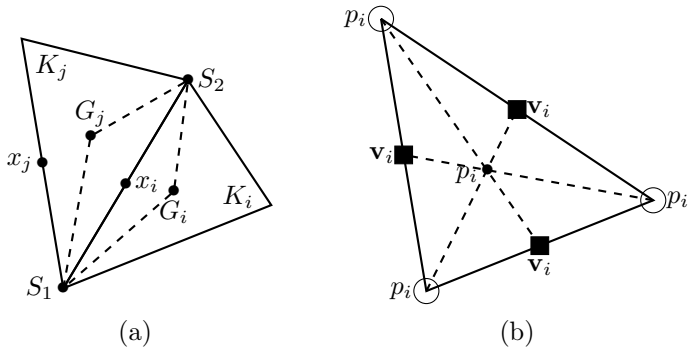

Figure 3: (a) Dual control volume between two adjacent triangular cells K_i and K_j of respective barycenters G_i and G_j. (b) Degrees of freedom of a 2D element (black squares for velocity $\mathbf{v}_i$, black dots and circles for pressure p_i).

Upstream-centered Scheme for Conservation Laws) is used to approximate the nonlinear convective term $[L(\mathbf{v}_i)]$ and a multi-step technique (projection-correction) is employed to solve equation (12), introducing an intermediate (predicted) velocity $\tilde{\mathbf{v}}_i$ computed from

$$J^{n+1}\left([M] - [A] + [L({\mathbf{v}_i}^n)]\right)\tilde{\mathbf{v}}_i = [M]J^n{\mathbf{v}_i}^n + J^{n+1}[L({\mathbf{v}_i}^n)]\mathbf{v}^n_{i,ALE} - J^{n+1}[G]{p_i}^n. \quad (13)$$

The mass equation (12a) is then enforced by solving a Poisson equation for the pressure

$$[D][M]^{-1}[G]{p_i}' = [D]\tilde{\mathbf{v}}_i, \quad (14)$$

and the velocity is updated using the predicted velocity $\tilde{\mathbf{v}}_i$ and the pressure increment ${p_i}'$

$${\mathbf{v}_i}^{n+1} = \tilde{\mathbf{v}}_i - [M]^{-1}[G]{p_i}', \quad {p_i}^{n+1} = {p_i}^n + {p_i}'. \quad (15)$$

3.3. Extraction of the modal added-mass coefficients

For $KC \to 0$, the convective term of the dimensionless Navier-Stokes equations is negligible so that the fluid force is a linear combination of the cylinder velocity and acceleration. In our numerical simulations, the inner cylinder is applied a time sinusoidal displacement so that the component of the modal fluid force along the $\mathbf{e}_y$ direction writes

$$\Re\left\{\langle \mathbf{f}_i \cdot \mathbf{e}_y, w_j\rangle\right\} = \pi\left(m_{ij}\sin(t) - c_{ij}\cos(t)\right), \quad (16)$$

with m_{ij} and c_{ij} the dimensionless added-mass and damping coefficients, respectively. Introducing the Fourier inner product

$$[f, g] = \frac{1}{\pi}\int_0^{2\pi} f(t)g(t)dt, \quad (17)$$

the dimensionless added-mass coefficient is extracted from the numerical modal fluid force by taking the projection of equation (16) onto the sine function, i.e.

$$m_{ij} = \frac{1}{N_j}\frac{1}{\pi}[\sin(t), \Re\left\{\langle \mathbf{f}_i \cdot \mathbf{e}_y, w_j\rangle\right\}]. \quad (18)$$

3.4. Parameters for the numerical simulations

The numerical domain is composed of two coaxial oscillating cylinders C_j, with radii R_j and lengths L_j, see Fig. 4. The boundary conditions on the numerical domain consist of imposed displacement on the inner cylinder (red boundary) of the form $\mathbf{Q}(X)\sin(\Omega T)$, zero pressure on In and Out boundaries, and zero velocity on the wall boundaries. All simulations are performed with an imposed displacement of amplitude $Q = K(R_2 - R_1)$, with

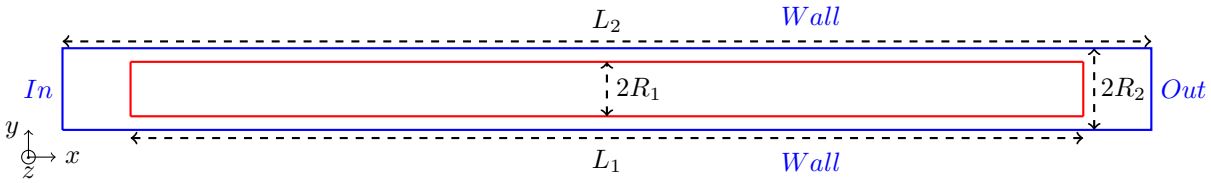

Figure 4: Illustration of the numerical fluid domain. Cut in the (x, y) plane.

$K = 2.5$ %, leading to a Keulegan-Carpenter number $KC \in \{0.9375, 2.5, 5\} \times 10^{-3}$ for $\varepsilon \in \{1.0375, 1.1, 1.2\}$. Adapting the amplitude of the imposed displacement to the size of the annulus makes it possible to keep a sufficiently small $K = KC/(\varepsilon - 1)$ number to minimize the nonlinear term of the Navier-Stokes equations, see equation (9). In our numerical simulations, the dimensionless rotational displacement θ_i of the cross-sections is taken into account. However, for an elongated cylinder, i.e. $l >> 1$, this displacement, which scales as $1/l$, has no significant effect on the added-mass coefficients. The forcing frequency is $\Omega/(2\pi) = 90$ Hz, leading to a Stokes number $Sk = 2.3 \times 10^4$. For $\varepsilon \in \{1.0375, 1.1, 1.2\}$, such a Stokes number makes it possible to minimize the viscous term which scales as $Sk^{-1}(\varepsilon - 1)^{-2}$.

The iterative solver GMRES from the PETSc library solves the linear system (13). PETSc GCP with SSOR preconditioning solves the systems (11) and (14). To discretize the fluid domain, we use an unstructured grid of tetrahedrons generated with the SALOME-platform. The mesh is decomposed into several partitions using the integrated METIS software. In TrioCFD, the parallel computing performance is optimized when each processor core has about $25000 - 30000$ tetrahedral cells. The transfer and communication between cores processors use the standard MPI (Message Passing Interface) library.

4. Position of the problem

To concretely introduce the issue which is the subject of the present study, we consider the case in which the inner cylinder is imposed a vibration mode corresponding to a clamped-free boundary condition, i.e.

$$w_i(x) = \cosh(\lambda_i x) - \cos(\lambda_i x) - \sigma_i(\sinh(\lambda_i x) - \sin(\lambda_i x)). \tag{19}$$

In this equation, λ_i is the dimensionless wave-number of the mode and is given by the $i-th$ solution of the transcendental equation $\cosh(\lambda)\cos(\lambda) + 1 = 0$. The parameter $\sigma_i = (\cosh(\lambda) + \cos(\lambda))(\sinh(\lambda) + \sin(\lambda))^{-1}$ is defined in terms of λ_i to satisfy the boundary conditions $w_i(0) = dw_i/dx(0) = d^2w_i/dx^2(1) = d^3w_i/dx^3(1) = 0$.

In the slender-body theory, the cylinder is modeled as a set of infinitesimal rigid elements of dimensionless length dx, subject to a dimensionless fluid force $df_i(x) = f_i(x)dx$ with $f_i(x)$ the dimensionless linear force. A 2D potential fluid flow theory, see [10, 5], shows that this dimensionless linear fluid force is proportional to the local acceleration of the mode, i.e. $f_i = \pi m_0 w_i$ with

$$m_0(\varepsilon) = \frac{\varepsilon^2 + 1}{\varepsilon^2 - 1}. \tag{20}$$

The coefficient m_0 does not depend on the dimensionless wave-number λ_i of the imposed mode, nor on the aspect ratio l of the vibrating cylinder, but only on the radius ratio ε, which acts as a confinement parameter. As we will see in §Appendix C, m_0 is the dimensionless added-mass of an infinitely long cylinder subject to a rigid mode of vibration. From equation (7), it follows that the dimensionless added-mass is

$$m_{ij}^{(\mathrm{ref},\infty)}(\varepsilon) = \frac{\varepsilon^2 + 1}{\varepsilon^2 - 1}\frac{\langle w_i, w_i\rangle}{N_i^2}\delta_{ij}. \tag{21}$$

A straightforward and important consequence that arises from the slender-body theory is that the added-mass matrix (21) is purely diagonal, meaning that the fluid does not couple modes with different wave-numbers.
To check the limits of validity of the slender-body theory, we have carried out 3D numerical simulations of the clamped-free case, using TrioCFD. The simulations are performed with $R_1 = 0.02$ m, $R_2 = 0.022$ m, $L = 0.7$ m,

Clamped – **Free**	Slender − body theory, $m_{ij}^{(\mathrm{ref},\infty)}$			Numerics TrioCFD			Relative deviation (%)
	$\begin{pmatrix} 2.631 & 0 & 0 \\ 0 & 2.631 & 0 \\ 0 & 0 & 2.631 \end{pmatrix}$			$\begin{pmatrix} 2.475 & 0.2391 & -0.2067 \\ 0.2405 & 2.463 & 0.2232 \\ -0.2081 & 0.2241 & 2.410 \end{pmatrix}$			10 .0

Table 1: Dimensionless added-mass matrix for the clamped-free case. The radius ratio is $\varepsilon = 1.1$ and the aspect ratio is $l = 35$. The added-mass from the slender-body theory is given by the equation (21).

so that the aspect ratio and the radius ratio are $l = 35$ and $\varepsilon = 1.1$, respectively. The amplitude of the imposed displacement is $Q = 5 \times 10^{-5}$ m, leading to a Keulegan-Carpenter number $KC = 2.5 \times 10^{-3}$. For $\varepsilon = 1.1$, such a Keulegan-Carpenter number makes it possible to minimize the nonlinear term of the Navier-Stokes equations, which scales as $KC/(\varepsilon - 1)$, see equation (9). The forcing frequency is $\Omega/(2\pi) = 90$ Hz, leading to a Stokes number $Sk = 2.3 \times 10^4$. For $\varepsilon = 1.1$, such a Stokes number makes it possible to minimize the viscous term of the Navier-Stokes equation, which scales as $Sk^{-1}(\varepsilon - 1)^{-2}$, see equation (9). In this simulation, and in all the following ones, we only consider the first three modes of vibration, i.e. $i \in [\![1, 3]\!]$. The results of this simulation are presented in Table 1.

We observe that the numerical added-mass matrix is non-diagonal, with off-diagonal terms of the order of 10% of the diagonal terms. We conclude that the slender-body theory, which does not account for the aspect ratio of the cylinder nor the wave-number of the vibration mode, is a good approximation to estimate the diagonal terms (the maximum relative deviation from the simulation is 10%), but is unsuitable for estimating the off-diagonal coefficients. This observation is of particular importance as it may noticeably affect the classical analyses of stability of beams in axial flows. Note that the three-dimensional approximate potential theory of [16], where the axial mode shape is arbitrarily imposed in the form of a sine function, makes it possible to take into account the aspect ratio of the cylinder and the wave-number of the vibration mode in the prediction of the diagonal coefficients. However, like the slender-body theory, it does not make it possible to reproduce the off-diagonal terms.

To overcome this issue, we now present a new theoretical formulation based on the assumption of a narrow fluid annulus. We also consider that the flexible cylinder is sufficiently elongated, i.e. $l >> 1$, so that we can neglect the rotational displacement θ_i of the cross-sections.

5. Theoretical model for the added-mass matrix

In our theoretical approach, we consider that the viscous effects are negligible compared with the inertia of the fluid. This corresponds to the asymptotic limit $Sk \to \infty$ in the dimensionless Navier-Stokes equations (9). In the limit of small oscillations, i.e. $KC \to 0$, the nonlinear convective term is also negligible, so that equation (9) simplifies to

$$\nabla^* \cdot \mathbf{v}_i = 0, \tag{22a}$$

$$\mathrm{i}\mathbf{v}_i + \frac{1}{\varepsilon - 1}\nabla^* p_i = \mathbf{0}, \tag{22b}$$

$$(\mathbf{v}_i - \mathrm{i}\mathbf{q}_i) \cdot \mathbf{n}_1 = 0 \quad \text{on } \partial C_1, \tag{22c}$$

$$\mathbf{v}_i \cdot \mathbf{n}_2 = 0 \quad \text{on } \partial C_2. \tag{22d}$$

In this formulation, the viscous boundary conditions given in equation (9) have been replaced by their invsiscid counterparts which ensure the continuity of the normal velocities at the boundaries of the cylinders. The divergence of equation (22b) shows that the pressure field is a harmonic function

$$\Delta^* p_i = \frac{\partial^2 p_i}{\partial r^2} + \frac{1}{r}\frac{\partial p_i}{\partial r} + \frac{1}{r^2}\frac{\partial^2 p_i}{\partial \theta^2} + \frac{1}{l^2}\frac{\partial^2 p_i}{\partial x^2} = 0, \tag{23}$$

with $(r, \theta, x) = (R/R_1, \theta, X/L)$ the dimensionless cylindrical coordinates. Changing variable r to $\tilde{r}$ defined as $\tilde{r} = r - 1$, introducing $\tilde{p}_i(\tilde{r}, \theta, x) = p_i(r - 1, \theta, x)$ and restricting the analysis to a narrow annulus, where $1/r \approx 1$, the Laplace equation (23) approximates to

$$\frac{\partial \tilde{p}_i}{\partial \tilde{r}} + \frac{\partial^2 \tilde{p}_i}{\partial \theta^2} + \frac{1}{l^2}\frac{\partial^2 \tilde{p}_i}{\partial x^2} = -\frac{\partial^2 \tilde{p}_i}{\partial \tilde{r}^2}. \tag{24}$$

Averaging equation (24) in the radial direction of the annulus yields

$$\left\langle \frac{\partial \tilde{p_i}}{\partial \tilde{r}} \right\rangle_{\tilde{r}} + \frac{\partial^2 \langle \tilde{p_i} \rangle_{\tilde{r}}}{\partial \theta^2} + \frac{1}{l^2} \frac{\partial^2 \langle \tilde{p_i} \rangle_{\tilde{r}}}{\partial x^2} = -\frac{1}{\varepsilon - 1} \left[\frac{\partial \tilde{p_i}}{\partial \tilde{r}} \right]_{\tilde{r}=0}^{\tilde{r}=\varepsilon-1}, \tag{25}$$

with $\langle \tilde{p_i} \rangle_{\tilde{r}} = \frac{1}{\epsilon - 1} \int_0^{\varepsilon-1} \tilde{p_i} d\tilde{r}$. The first left hand side term writes $\left\langle \frac{\partial \tilde{p_i}}{\partial r} \right\rangle = \frac{1}{\varepsilon - 1} \left(\tilde{p_i} \left(\varepsilon - 1 \right) - \tilde{p_i} \left(0 \right) \right)$. Assuming that the pressure fluctuation $\tilde{p_i}(\varepsilon - 1) - \tilde{p_i}(0)$ is small compared with the average pressure $\langle \tilde{p_i} \rangle$ in the narrow annulus, this term is negligible compared to the second left hand side term of equation (25). The right hand side term is obtained from the projection of equation (22b) on $\mathbf{e}_r = -\mathbf{n}_2$. Using the boundary conditions (22c) and (22d) one obtains

$$\left. \frac{\partial \tilde{p_i}}{\partial \tilde{r}} \right|_{\tilde{r}=0} = -\mathrm{i} \mathbf{v}_i \cdot \mathbf{e}_r \approx -\mathrm{i} \mathbf{v}_i \cdot \mathbf{n}_1 = \frac{w_i}{N_i} \cos \left(\theta \right), \quad \left. \frac{\partial \tilde{p_i}}{\partial \tilde{r}} \right|_{\tilde{r}=\varepsilon-1} = 0, \tag{26}$$

where the approximation $\mathbf{e}_r \approx \mathbf{n}_1$ is supported by the assumption of small oscillations, i.e. $KC = o(1)$. Seeking a solution as $\langle \tilde{p_i} \rangle_{\tilde{r}} = \overline{p_i} \left(x \right) / N_i \cos \left(\theta \right)$, the equation (25) finally approximates to

$$\frac{d^2 \overline{p_i}}{dx^2} - l^2 \overline{p_i} = \frac{1}{\varepsilon - 1} l^2 w_i. \tag{27}$$

The forcing term w_i on the right hand side of equation (27) represents the bending mode of vibration which is imposed to the inner cylinder. Modeling this cylinder as an Euler-Bernoulli beam, w_i is a linear combination between trigonometric and hyperbolic functions,

$$w_i \left(x \right) = \chi^{(1)} \cosh \left(\lambda_i x \right) + \chi^{(2)} \cos \left(\lambda_i x \right) + \chi_i^{(3)} \sinh \left(\lambda_i x \right) + \chi_i^{(4)} \sin \left(\lambda_i x \right), \tag{28}$$

with $\chi^{(k)}$ some real coefficients which depend on the type of boundary conditions applied at the ends of the beam. Considering the usual boundary conditions listed in Table A.6, the coefficients $\chi_i^{(3)}$ and $\chi_i^{(4)}$ may depend on the wave-number λ_i of the vibration mode and are consequently indexed with a subscript i. To simplify the following developments, we write the modal displacement on a compact form, $w_i = \sum_{k=1}^{2} w_i^{(k)}$ with

$$w_i^{(k)} \left(x \right) = \chi^{(k)} \cos \left(\mathrm{i}^k \lambda_i x \right) + \chi_i^{(k+2)} (-\mathrm{i})^k \sin \left(\mathrm{i}^k \lambda_i x \right). \tag{29}$$

From the linearity of equation (27), the dimensionless pressure term $\overline{p_i}$ writes $\overline{p_i} = \sum_{k=1}^{2} \overline{p_i}^{(k)}$ with $\overline{p_i}^{(k)}$ satisfying

$$\frac{d^2 \overline{p_i}^{(k)}}{dx^2} - l^2 \overline{p_i}^{(k)} = \frac{1}{\varepsilon - 1} l^2 w_i^{(k)}. \tag{30}$$

The solution of this linear equation is the sum of the solution of the homogeneous equation and a particular solution sought as a superposition of cosine and sine functions. This yields

$$\overline{p_i}^{(k)} \left(x \right) = -\left[g_i^{(k)} \left(x, l, \varepsilon \right) + a_i^{(k)} \left(l, \varepsilon \right) \mathrm{e}^{lx} + b_i^{(k)} \left(l, \varepsilon \right) \mathrm{e}^{-lx} \right], \tag{31}$$

with

$$g_i^{(k)} \left(x, l, \varepsilon \right) = \frac{1}{\varepsilon - 1} \frac{1}{1 + (-1)^k (\lambda_i / l)^2} w_i^{(k)} \left(x \right). \tag{32}$$

The functions $a_i^{(k)}$ and $b_i^{(k)}$ are determined with the dimensionless pressure conditions at both ends of the beam, namely $\overline{p_i}(0)$ and $\overline{p_i}(1)$

$$a_i^{(k)} \left(l, \varepsilon \right) + b_i^{(k)} \left(l, \varepsilon \right) = -\left[\overline{p_i}^{(k)} \left(0 \right) + g_i^{(k)} \left(0, l, \varepsilon \right) \right], \tag{33a}$$

$$a_i^{(k)} \left(l, \varepsilon \right) \mathrm{e}^{l} + b_i^{(k)} \left(l, \varepsilon \right) \mathrm{e}^{-l} = -\left[\overline{p_i}^{(k)} \left(1 \right) + g_i^{(k)} \left(1, l, \varepsilon \right) \right]. \tag{33b}$$

Solving the linear system (33) yields

$$a_i^{(k)} \left(l, \varepsilon \right) = b_i^{(k)} \left(-l, \varepsilon \right) = \frac{\left[g_i^{(k)} \left(0, l, \varepsilon \right) + \overline{p_i}^{(k)} \left(0 \right) \right] \mathrm{e}^{-l} - \left[g_i^{(k)} \left(1, l, \varepsilon \right) + \overline{p_i}^{(k)} \left(1 \right) \right]}{2 \sinh \left(l \right)}, \tag{34}$$

so that the dimensionless pressure $\overline{p_i}^{(k)}$ generated by $w_i^{(k)}$ writes

$$\overline{p_i}^{(k)} \left(x \right) = -\left[g_i^{(k)} \left(x, l, \varepsilon \right) + \sum_{n=1}^{2} a_{in}^{(k)} \left(l, \varepsilon \right) \mathrm{e}^{(-1)^n lx} \right], \tag{35}$$

with $a_{in}^{(k)}(l,\varepsilon) = a_i^{(k)}((-1)^n l,\varepsilon)$, i.e.

$$a_{in}^{(k)}(l,\varepsilon) = \frac{(-1)^n}{2}\frac{g_i^{(k)}(0,l,\varepsilon)}{\mathrm{e}^{(-1)^n l}\sinh(l)} + \frac{(-1)^{n+1}}{2}\frac{g_i^{(k)}(1,l,\varepsilon)}{\sinh(l)} + \frac{(-1)^n}{2}\frac{\overline{p_i}^{(k)}(0)}{\mathrm{e}^{(-1)^n l}\sinh(l)} + \frac{(-1)^{n+1}}{2}\frac{\overline{p_i}^{(k)}(1)}{\sinh(l)}. \quad (36)$$

The first two terms in equation (36) scale as $(\varepsilon-1)^{-1}$ and thus are predominant over the last two terms for a narrow annulus. Injecting equation (32) in equation (36) yields

$$a_{in}^{(k)}(l,\varepsilon) \underset{\varepsilon\to 1}{\sim} \frac{1}{\varepsilon-1}\frac{1}{1+(-1)^k(\lambda_i/l)^2}\frac{(-1)^n \mathrm{e}^{(-1)^{n+1}\frac{l}{2}}}{2\sinh(l)}\left[w_i^{(k)}(0)\,\mathrm{e}^{(-1)^{n+1}\frac{l}{2}} - w_i^{(k)}(1)\,\mathrm{e}^{-(-1)^{n+1}\frac{l}{2}}\right]. \quad (37)$$

The dimensionless modal added-mass coefficient m_{ij} is obtained from the projection of the dimensionless linear fluid force $-\overline{p_i}^{(k)}/N_i\cos(\theta)$ generated by the i-th normalized mode w_i/N_i onto the j-th normalized mode w_j/N_j, leading to

$$m_{ij}(l,\varepsilon) = \frac{1}{\varepsilon-1}\left[m_{ij}^{(S)}(l) + m_{ij}^{(A)}(l,\varepsilon)\right], \quad (38)$$

with

$$m_{ij}^{(S)}(l) = \frac{1}{N_i N_j}\sum_{k=1}^{2}\frac{1}{1+(-1)^k(\lambda_i/l)^2}\sum_{q=1}^{2} m_{ij}^{(kq)} \qquad \text{where} \qquad m_{ij}^{(kq)} = \left\langle w_i^{(k)}, w_j^{(q)}\right\rangle, \quad (39a)$$

$$m_{ij}^{(A)}(l,\varepsilon) = \frac{\varepsilon-1}{N_i N_j}\sum_{k=1}^{2}\sum_{q=1}^{2}\sum_{n=1}^{2} a_{in}^{(k)}(l,\varepsilon)\, m_{nj}^{(q)}(l) \qquad \text{where} \qquad m_{nj}^{(q)}(l) = \left\langle \mathrm{e}^{(-1)^n lx}, w_j^{(q)}(x)\right\rangle, \quad (39b)$$

$$\underset{\varepsilon\to 1}{\sim} \frac{1}{N_i N_j}\sum_{k=1}^{2}\frac{1}{1+(-1)^k(\lambda_i/l)^2}\sum_{q=1}^{2}\sum_{n=1}^{2}(-1)^n\frac{\mathrm{e}^{(-1)^{n+1}\frac{l}{2}}}{2\sinh(l)}\begin{bmatrix} w_i^{(k)}(0)\,\mathrm{e}^{(-1)^{n+1}\frac{l}{2}} \\ -w_i^{(k)}(1)\,\mathrm{e}^{-(-1)^{n+1}\frac{l}{2}}\end{bmatrix} m_{nj}^{(q)}(l). \quad (39c)$$

The term $\left[1+(-1)^k(\lambda_i/l)^2\right]^{-1}$ in equation (39) clearly indicates that the fluid has a different effect on the hyperbolic ($k=1$) and trigonometric ($k=2$) parts of the imposed vibration mode. Thus, it is expected that the fluid will deform the vibration modes which are linear combinations of these two parts, subsequently leading to nonzero off-diagonal added-mass coefficients. As we shall see in §Appendix D, among all the tested configurations listed in Table A.6, the pinned-pinned case is the only one which has a pure trigonometric (sine) vibration mode satisfying the same boundary conditions as the pressure field, i.e. $\overline{p_i}^{(k)}(0) = \overline{p_i}^{(k)}(1) = 0$, these two terms being neglected in equation (36) under the assumption of a narrow annulus. Consequently, this configuration is expected to yield zero off-diagonal added-mass coefficients, whatever the confinement and the aspect ratio.

The formulation (38), which has been derived from the assumption of a narrow annulus, applies for all the boundary conditions listed in Table A.6, by selecting the adequate coefficients $\chi^{(k)}$ and $\chi^{(k+2)}$ in equation (28) and by computing the terms $m_{ij}^{(kq)}$ and $m_{nj}^{(q)}$ in equation (39). Full analytical expressions for these terms are provided in Appendix B. These expressions, based on an index notation, can easily be implemented in any numeric computing environment.

5.1. Slender-body limit, $l\to\infty$

The added-mass of an infinitely long cylinder is obtained by taking the limit of equation (39) as $l\to\infty$. It yields

$$m_{ij}^{(S)}(l) \underset{l\to\infty}{\to} \frac{\langle w_i, w_i\rangle}{N_i^2}\delta_{ij}, \quad m_{ij}^{(A)}(l,\varepsilon) \underset{l\to\infty}{\to} 0, \quad (40)$$

so that equation (38) simplifies to

$$m_{ij}(l,\varepsilon) \underset{l\to\infty}{\to} m_{ij}^{(\infty)}(\varepsilon) = \frac{1}{\varepsilon-1}\frac{\langle w_i, w_i\rangle}{N_i^2}\delta_{ij}. \quad (41)$$

The equation (41) shows that the added-mass matrix of an infinitely long cylinder is diagonal, as expected from the slender-body theory. However, note that equation (41) differs from equation (21) by a factor $m_{ij}^{(\infty)}/m_{ij}^{(\mathrm{ref},\infty)} = (\varepsilon+1)(\varepsilon^2+1)^{-1}$ whose evolution is shown in Fig. 5. In this figure, we show that the two approaches are actually equivalent for small values of the radius ratio, i.e. $\varepsilon < 1.2$, but rapidly differ as ε increases (the two theories differ by more than 10% for $\varepsilon > 1.2$). We explain this difference from the fact that our theory has been developed under the assumption of a narrow annulus, and as such is restricted to radius ratios close to unity.

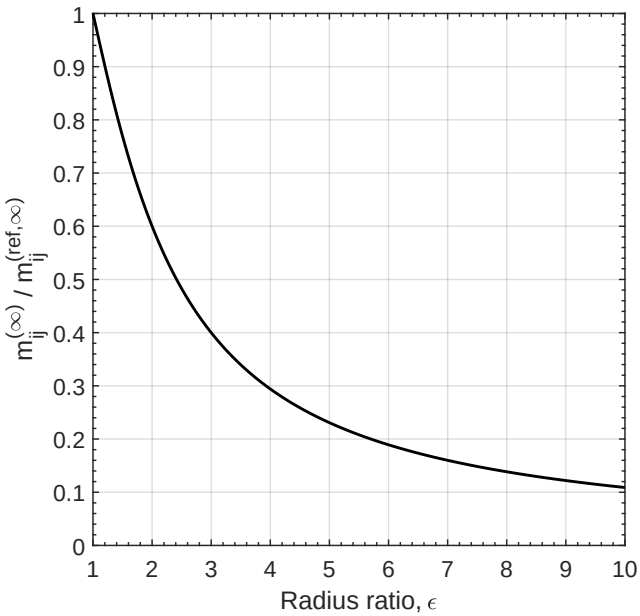

Figure 5: Evolution of the ratio $m_{ij}^{(\infty)}/m_{ij}^{(\mathrm{ref},\infty)} = (\varepsilon+1)(\varepsilon^2+1)^{-1}$ as a function of the radius ratio ε.

6. Results for the added-mass matrix

In the previous section we have presented a new theoretical formulation to estimate the added-mass matrix of a finite size cylinder vibrating in a confined environment. In this section, we show the results of this theory, considering different boundary conditions, aspect ratios and radius ratios. Note that the Table A.6 provides all the necessary parameters needed to compute the added-mass matrix from equation (38). In particular the second column gives the value of the $\chi^{(k)}$ and $\chi^{(k+2)}$ parameters introduced in the linear combination (29) to switch from one boundary condition case to another.

6.1. Effect of the boundary conditions and the aspect ratio

In this section, we analyze the variations of the added-mass coefficients for various boundary conditions of the flexible inner cylinder and a range of aspect ratios $l \in [10, 200]$. In the core of the manuscript, we show the results for the free-free, clamped-sliding, clamped-pinned, clamped-free and pinned-pinned cases. The rigid and clamped-clamped cases, which have already been solved by [19] and [18] are discussed in Appendix C and Appendix D. The free-sliding, free-pinned, sliding-pinned and sliding-sliding cases, which do not bring additional information in the analysis are reported in Appendix E.

In Figs. 6 to 10, we show the theoretical evolution of the diagonal and off-diagonal terms $(\epsilon-1)m_{ij}$ as a function of the aspect ratio l, for $i, j \in [\![1, 3]\!]$. Note that such a representation is independent of the radius ratio ε, which makes these figures very general and usable for any case of confinement.

First, we observe that the diagonal terms are monotonic increasing functions of the aspect ratio. Here again, from a physical point of view, it means that the modal frequency of oscillation of a flexible cylinder free to vibrate in a fluid at rest is all the greater as the cylinder is long, and that whatever the boundary conditions. Also, we recover that the diagonal terms tend to the asymptotic limit $m_{ij}^{(\infty)}$ given by equation (41) as $l \to \infty$. With the exception of the clamped-clamped and clamped-sliding cases, $m_{ij}^{(\infty)}$ weakly depends on the wave-number of the vibration mode. Indeed the wave-number mainly influences the speed at which the coefficient approaches the limit, the coefficients associated with the smallest wave-number being faster. The clamped-clamped and clamped-sliding cases are exceptions in the sense that m_{11} has an asymptotic limit very different from the other diagonal terms. We have reported in Table F.8 of Appendix F the values of the asymptotic limits $(\varepsilon-1)\, m_{ij}^{(\infty)}$ for all the cases of boundary conditions.

Second, the off-diagonal terms exhibit very different variations depending on the type of boundary conditions and the wave-number of the modes. For example, in the case of a free-free configuration, the terms m_{31} and m_{13} are equal, negative, and are non-monotonic functions of the aspect ratio l. This non-monotonic behaviour indicates that the intensity of the coupling between the first and the third mode, via the fluid, strongly depends

on the aspect ratio. On the other hand, for the same configuration, the terms m_{12} and m_{21} are always zero, so that whatever the aspect ratio of the cylinder, the fluid is not able to couple the first mode of vibration with the second. A very different behaviour is observed for the clamped-pinned configuration, for which all the off-diagonal terms are monotonic positive decreasing functions of the aspect ratio. In such a case, the fluid actually deforms the vibration mode and generates a pressure field with a different shape as the imposed mode. In the case of a clamped-free configuration, the added-mass matrix is symmetric. The terms m_{13} and m_{31} are monotonic negatives, increasing functions of the aspect ratio l; whereas all the other off-diagonal terms are positive decreasing functions of l. We note that the pinned-pinned case is the only configuration for which all the off-diagonal terms equal zero. This results is actually a direct consequence of the fact that the pinned-pinned case is the only tested boundary condition for which the vibration mode is a pure trigonometric function (sine) satisfying the same boundary conditions as the pressure field, i.e. $\overline{p_i}^{(k)}(0) = \overline{p_i}^{(k)}(1) = 0$, these two terms being actually neglected in equation (36) under the assumption of a narrow annulus. It follows that the finite length of the cylinder only affects the diagonal terms of the added-mass matrix. This conclusion applies not only to the pinned-pinned modes but to all wet modes, i.e., modes that satisfy the same boundary conditions as the pressure field at $x = 0$ and $x = 1$, that's to say $w_i(0) = w_i(1) = 0$. These wet modes are solutions to an eigenvalue problem that takes into account the presence of the surrounding fluid, contrarily to the dry modes listed in Table A.6 and studied in the present manuscript.

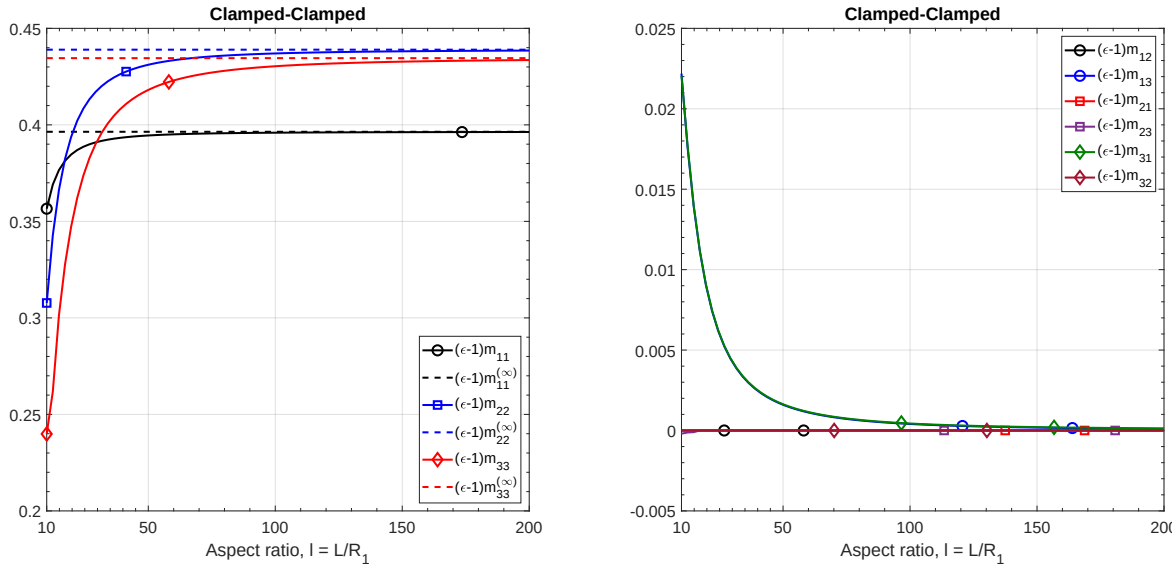

Figure 6: Clamped-Clamped case. Evolution of the added-mass coefficient $(\varepsilon - 1)m_{ij}$, predicted by the equation (38), as a function of the aspect ratio l. Left : diagonal terms. The horizontal dashed lines correspond to the limit $l \to \infty$, given by the equation (41). Right : off-diagonal terms. These terms tend to 0 as $l \to \infty$. Symbols are used to distinguish superimposed curves.

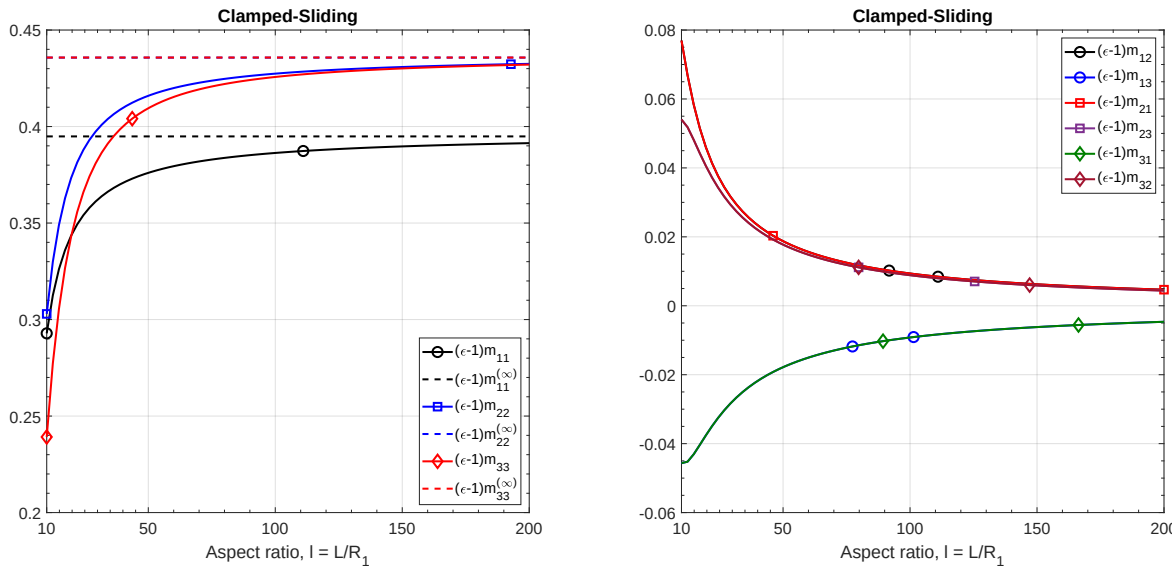

Figure 7: Clamped-Sliding case. Evolution of the added-mass coefficient $(\varepsilon - 1)m_{ij}$, predicted by the equation (38), as a function of the aspect ratio l. Left : diagonal terms. The horizontal dashed lines correspond to the limit $l \to \infty$, given by the equation (41). Right : off-diagonal terms. These terms tend to 0 as $l \to \infty$. Symbols are used to distinguish superimposed curves.

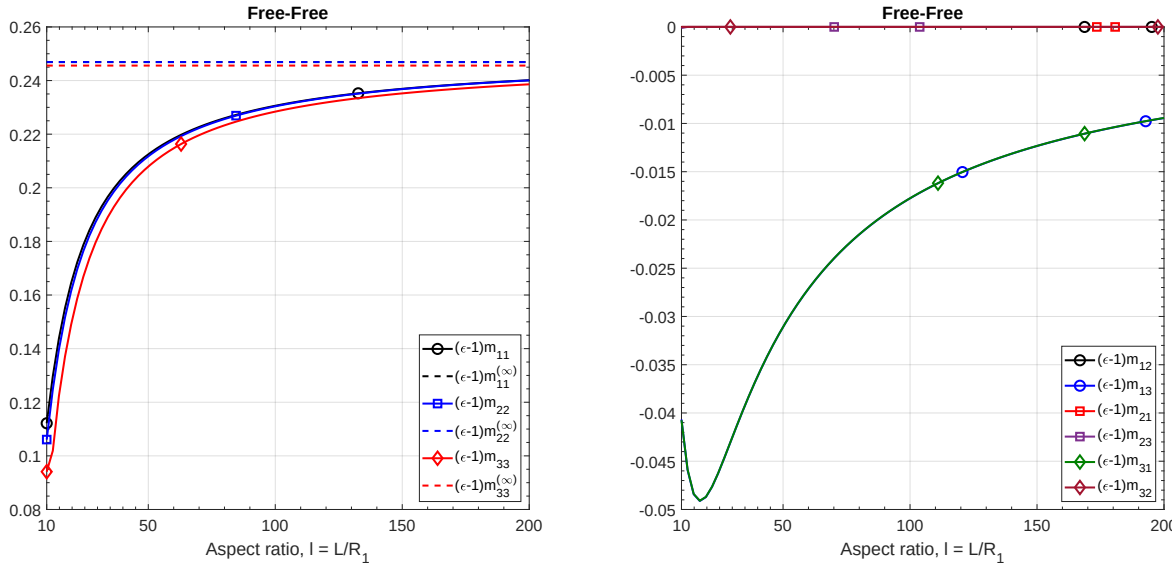

Figure 8: Free-Free case. Evolution of the added-mass coefficient $(\varepsilon - 1)m_{ij}$, predicted by the equation (38), as a function of the aspect ratio l. Left : diagonal terms. The horizontal dashed lines correspond to the limit $l \to \infty$, given by the equation (41). Right : off-diagonal terms. These terms tend to 0 as $l \to \infty$. Symbols are used to distinguish superimposed curves.

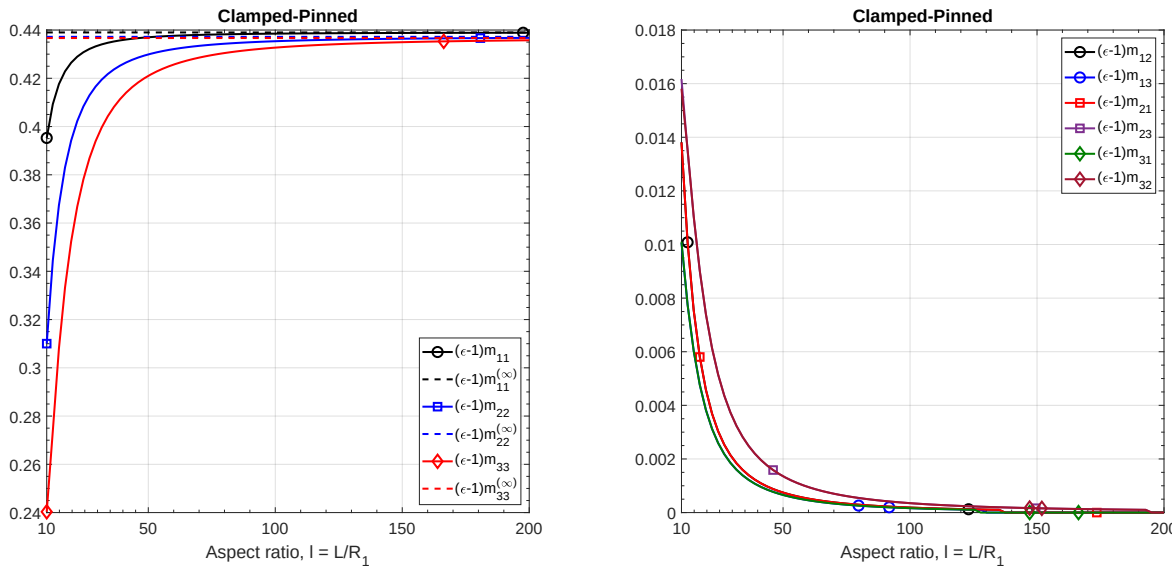

Figure 9: Clamped-Pinned case. Evolution of the added-mass coefficient $(\varepsilon - 1)m_{ij}$, predicted by the equation (38), as a function of the aspect ratio l. Left : diagonal terms. The horizontal dashed lines correspond to the limit $l \to \infty$, given by the equation (41). Right : off-diagonal terms. These terms tend to 0 as $l \to \infty$. Symbols are used to distinguish superimposed curves.

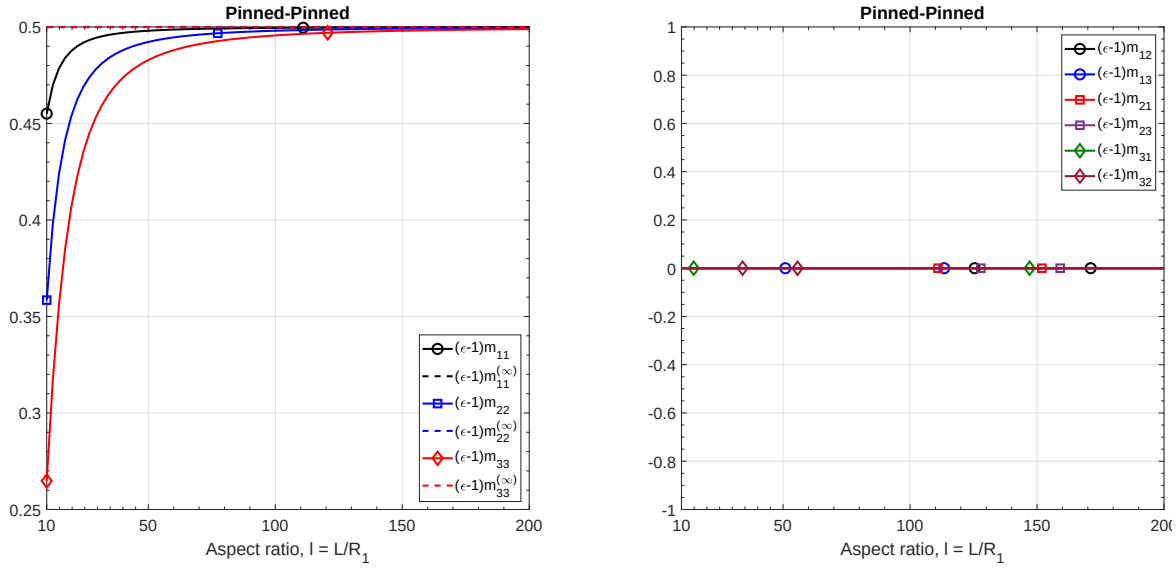

Figure 10: Pinned-Pinned case. Evolution of the added-mass coefficient $(\varepsilon - 1)m_{ij}$, predicted by the equation (38), as a function of the aspect ratio l. Left : diagonal terms. The horizontal dashed lines correspond to the limit $l \to \infty$, given by the equation (41). Right : off-diagonal terms. These terms tend to 0 as $l \to \infty$. Symbols are used to distinguish superimposed curves.

Pinned – **Pinned**	Present theory	Numerics TrioCFD	Relative deviation (%)
$l = 35$	$\begin{pmatrix} 4.960 & 0 & 0 \\ 0 & 4.844 & 0 \\ 0 & 0 & 4.662 \end{pmatrix}$	$\begin{pmatrix} 5.430 & 0 & 0 \\ 0 & 5.294 & 0 \\ 0 & 0 & 5.081 \end{pmatrix}$	8.60
$l = 70$	$\begin{pmatrix} 4.990 & 0 & 0 \\ 0 & 4.960 & 0 \\ 0 & 0 & 4.911 \end{pmatrix}$	$\begin{pmatrix} 5.461 & 0 & 0 \\ 0 & 5.426 & 0 \\ 0 & 0 & 5.368 \end{pmatrix}$	8.62
$l = 140$	$\begin{pmatrix} 4.997 & 0 & 0 \\ 0 & 4.990 & 0 \\ 0 & 0 & 4.977 \end{pmatrix}$	$\begin{pmatrix} 5.498 & 0 & 0 \\ 0 & 5.489 & 0 \\ 0 & 0 & 5.474 \end{pmatrix}$	9.11

Table 2: Dimensionless added-mass matrix for the pinned-pinned case and three values of the aspect ratio $l = \{35, 70, 140\}$. The added-mass from the present theory is given by the equation (38). The radius ratio is $\varepsilon = 1.1$. The last column gives the maximum relative deviation on the diagonal terms.

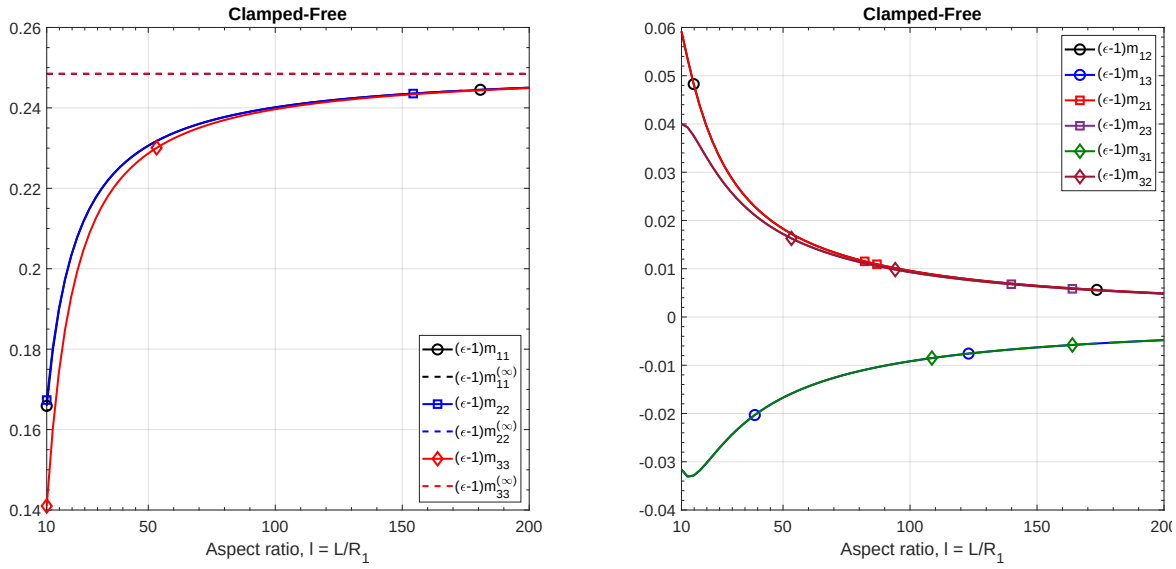

Figure 11: Clamped-Free case. Evolution of the added-mass coefficient $(\varepsilon - 1)m_{ij}$, predicted by the equation (38), as a function of the aspect ratio l. Left : diagonal terms. The horizontal dashed lines correspond to the limit $l \to \infty$, given by the equation (41). Right : off-diagonal terms. These terms tend to 0 as $l \to \infty$. Symbols are used to distinguish superimposed curves.

Clamped – **Free**	Present theory	Numerics TrioCFD	Relative deviation (%)
$l = 35$	$\begin{pmatrix} 2.227 & 0.2506 & -0.2190 \\ 0.2506 & 2.227 & 0.2287 \\ -0.2190 & 0.2287 & 2.189 \end{pmatrix}$	$\begin{pmatrix} 2.475 & 0.2391 & -0.2067 \\ 0.2405 & 2.463 & 0.2232 \\ -0.2081 & 0.2241 & 2.410 \end{pmatrix}$	10.0 5.95
$l = 70$	$\begin{pmatrix} 2.360 & 0.1341 & -0.1261 \\ 0.1341 & 2.360 & 0.1285 \\ -0.1261 & 0.1285 & 2.350 \end{pmatrix}$	$\begin{pmatrix} 2.603 & 0.1267 & -0.1191 \\ 0.1278 & 2.598 & 0.1238 \\ -0.1199 & 0.1243 & 2.584 \end{pmatrix}$	9.33 5.88
$l = 140$	$\begin{pmatrix} 2.429 & 0.06920 & -0.06720 \\ 0.06920 & 2.429 & 0.06780 \\ -0.06720 & 0.06780 & 2.427 \end{pmatrix}$	$\begin{pmatrix} 2.682 & 0.06520 & -0.06380 \\ 0.06590 & 2.681 & 0.06500 \\ -0.06390 & 0.06520 & 2.677 \end{pmatrix}$	10.2 5.70

Table 3: Dimensionless added-mass matrix for the clamped-free case and three values of the aspect ratio $l = \{35, 70, 140\}$. The added-mass from the present theory is given by the equation (38). The radius ratio is $\varepsilon = 1.1$. The first (resp. second) number given in the last column of the table corresponds to the maximum relative deviation on the diagonal (resp. off-diagonal) terms.

In Tables 2 and 3, we compare theoretical and numerical predictions for the added-mass matrix of the pinned-pinned and clamped-free cases, considering three values of the aspect ratio, $l \in \{35, 70, 140\}$. To keep the core of this manuscript light, we have reported in Appendix G the results for all other boundary conditions, which lead to conclusions similar to the two cases presented here.

The numerical simulations are performed with $R_1 = 0.02$ m and three different lengths for the inner cylinder, $L \in \{0.7, 1.4, 2.8\}$ m. The radius of the external cylinder is $R_2 = 0.022$ m, so that the radius ratio is $\varepsilon = 1.1$. We use a locally refined grid of tetrahedrons generated by the MGCADSurf-MGTetra mesh generator of the SALOME-platform. Two different local sizes were defined: a small local size of 5×10^{-4} m for elements close to the inner cylinder, and a large global size 8×10^{-4} m for other elements. For $l = 70$, the mesh is composed of 22 million tetrahedrons. For $l = 140$, the mesh is composed of 28 million tetrahedrons. The time step is 3×10^{-4} s, and the CPU time is approximately 10 minutes.

For the pinned-pinned case, we observe that the theoretical approach and numerical simulations yield diagonal positive added-mass coefficients, and that whatever the aspect ratio. As expected from Fig. 10, the added-mass coefficients slightly increase with the aspect ratio, i.e. as the vibrating cylinder becomes more and more slender. Note that, similarly to the clamped-clamped case studied in §Appendix D, when l varies from $l = 35$ to $l = 140$, the increase is rather limited as the added-mass coefficients quickly tend to the slender-body limit $m_{ij}^{(\infty)} = 5$, see Fig. 10 and Table F.8. The maximum relative deviation between both predictions is satisfying in the sense that it remains less than 10 % for the three values of the aspect ratio tested.

For the clamped-free case, the theoretical approach and numerical simulations show that the added-mass matrix is non-diagonal. The diagonal terms are positive, slightly depend on the wave-number of the vibration mode and increase with the aspect ratio, as expected from Fig. 11. The maximum relative deviation on the diagonal terms is less than 11 % for the three values of the aspect ratio tested. Regarding the off-diagonal terms, the numerical simulations confirm that m_{12}, m_{21}, m_{32} and m_{23} (resp. m_{13} and m_{31}) are positive and decrease (resp. negative and increase) with the aspect ratio, as predicted by the theory, see also Fig. 11. The maximum relative deviation on the off-diagonal terms is very satisfying as it remains less than 6 %.

For these two cases of boundary conditions, and all the others reported in Appendix G, the small values of the maximum relative deviation indicate that the theoretical predictions correctly reproduce the variations of the added-mass coefficients as the aspect ratio of the cylinder is varied, as was also the case when the confinement was varied. In particular, the present study clearly shows that the dry vibration modes generate off-diagonal terms that vanish in the slender-body limit, i.e. $l \to \infty$.

6.2. Effect of the radius ratio

Pinned – **Pinned**	Present theory	Numerics TrioCFD	Relative deviation (%)
$\varepsilon = 1.0375$	$\begin{pmatrix} 13.23 & 0 & 0 \\ 0 & 12.92 & 0 \\ 0 & 0 & 12.43 \end{pmatrix}$	$\begin{pmatrix} 14.12 & 0 & 0 \\ 0 & 13.86 & 0 \\ 0 & 0 & 13.17 \end{pmatrix}$	6.78
$\varepsilon = 1.1$	$\begin{pmatrix} 4.960 & 0 & 0 \\ 0 & 4.844 & 0 \\ 0 & 0 & 4.662 \end{pmatrix}$	$\begin{pmatrix} 5.430 & 0 & 0 \\ 0 & 5.294 & 0 \\ 0 & 0 & 5.081 \end{pmatrix}$	8.60
$\varepsilon = 1.2$	$\begin{pmatrix} 2.480 & 0 & 0 \\ 0 & 2.422 & 0 \\ 0 & 0 & 2.331 \end{pmatrix}$	$\begin{pmatrix} 2.779 & 0 & 0 \\ 0 & 2.708 & 0 \\ 0 & 0 & 2.587 \end{pmatrix}$	10.7

Table 4: Dimensionless added-mass matrix for the pinned-pinned case and three values of the radius ratio $\varepsilon = \{1.0375, 1.1, 1.2\}$. The added-mass from the present theory is given by the equation (38). The aspect ratio is $l = 35$. The last column gives the maximum relative deviation on the diagonal terms.

Clamped – **Free**	Present theory	Numerics TrioCFD	Relative deviation (%)
$\varepsilon = 1.0375$	$\begin{pmatrix} 5.939 & 0.6682 & -0.5841 \\ 0.6682 & 5.937 & 0.6098 \\ -0.5841 & 0.6098 & 5.838 \end{pmatrix}$	$\begin{pmatrix} 6.370 & 0.6695 & -0.5732 \\ 0.6576 & 6.324 & 0.6063 \\ -0.5724 & 0.6034 & 6.185 \end{pmatrix}$	6.11 3.20
$\varepsilon = 1.1$	$\begin{pmatrix} 2.227 & 0.2506 & -0.2190 \\ 0.2506 & 2.227 & 0.2287 \\ -0.2190 & 0.2287 & 2.189 \end{pmatrix}$	$\begin{pmatrix} 2.475 & 0.2391 & -0.2067 \\ 0.2405 & 2.463 & 0.2232 \\ -0.2081 & 0.2241 & 2.410 \end{pmatrix}$	10.0 5.95
$\varepsilon = 1.2$	$\begin{pmatrix} 1.114 & 0.1253 & -0.1095 \\ 0.1253 & 1.113 & 0.1143 \\ -0.1095 & 0.1143 & 1.095 \end{pmatrix}$	$\begin{pmatrix} 1.278 & 0.1164 & -0.09944 \\ 0.1172 & 1.269 & 0.1098 \\ -0.1007 & 0.1112 & 1.239 \end{pmatrix}$	12.8 8.73

Table 5: Dimensionless added-mass matrix for the clamped-free case and three values of the radius ratio $\varepsilon = \{1.0375, 1.1, 1.2\}$. The added-mass from the present theory is given by the equation (38). The aspect ratio is $l = 35$. The first (resp. second) number given in the last column of the table corresponds to the maximum relative deviation on the diagonal (resp. off-diagonal) terms.

In Tables 4 and 5, we compare theoretical and numerical predictions for the added-mass matrix of the pinned-pinned and clamped-free cases, considering three values of the radius ratio, $\varepsilon \in \{1.0375, 1.1, 1.2\}$. To keep the core of this manuscript light, we have reported in Appendix H the results for all other boundary conditions, which lead to conclusions similar to the two cases presented here.

The numerical simulations are performed with $R_1 = 0.02$ m and three different external radii, $R_2 \in \{0.02075, 0.022, 0.024\}$ m. The length of the inner cylinder is $L = 0.7$ m, so that the aspect ratio is $l = 35$. We use a locally refined grid of tetrahedrons generated by the MGCADSurf-MGTetra mesh generator of the SALOME-platform. Two different local sizes were defined: a small local size of 5×10^{-4} m for elements close to the inner cylinder, and a large global size of 8×10^{-4} m for other elements. For $\varepsilon = 1.0375$, i.e., the most confined configuration, the mesh is composed of 8.5 million tetrahedrons. For $\varepsilon = 1.1$, the mesh is composed of 15 million tetrahedrons. For $\varepsilon = 1.2$, the mesh is composed of 25.9 million tetrahedrons. The time step is 5×10^{-4} s, and the CPU time is approximately 5 minutes.

For the pinned-pinned case, we observe that the theoretical approach and numerical simulations yield diagonal positive added-mass matrices, and that whatever the confinement. As expected from the fact that the added-mass increases with the confinement, the diagonal terms increase as ε decreases. The maximum relative deviation between both predictions is shown to increase with the radius ratio, with a value of 10.7% for the least confined configuration. This increase is in part due to the fact that our theoretical approach is carried out under the assumption of a narrow annulus and as such loses precision when ε increases.

For the clamped-free case, both theoretical and numerical approaches yield non-diagonal symmetric matrices (in the limit of the digital precision), indicating that the fluid couples modes with different wave-numbers. The diagonal terms are always positive whereas the sign of the off-diagonal terms depends on the wave-number of the vibration modes, as also shown in Fig. 11. Here again, similarly to the pinned-pinned case, we recover the fact that the added-coefficients, at least in absolute value, decrease as ε increases.

For these two cases of boundary conditions, and all the others reported in Appendix H, the small values of the maximum relative deviation indicate that the theoretical predictions are in good agreement with the numerical simulations, as long as the annular duct remains narrow enough. A detailed discussion on the differences between the theoretical and numerical approaches is reported in the next section.

7. Discussion on theory versus numerics

To explain the relative deviation between theoretical and numerical predictions, we identify three possible causes.

First, the theoretical approach is fully linear and inviscid since the convective and viscous terms of the Navier–Stokes equations are neglected. In our numerical simulations, these two terms are nonzero even if they are retained as small as possible by adapting the amplitude of the displacement to the size of the annulus and by using a large vibration frequency. Still, the nonlinear term may create secondary Fourier harmonics, which would affect the value of the added-mass coefficient extracted numerically; a small part of the damping coefficient c_{ij} defined in equation (16) being reflected in m_{ij}. This effect is illustrated in Fig. 12 which shows the time

evolution of the numerical dimensionless modal fluid force when a large amplitude of vibration ($Q = 5 \times 10^{-5}$ m, i.e. $KC = 2.5 \times 10^{-3}$) is imposed in a very narrow annulus ($R_2 - R_1 = 0.002$ m, i.e. $\varepsilon = 1.0375$). In this simulation, the nonlinear term of the Navier-Stokes equations is of order $KC/(\epsilon - 1) \approx 6.6$ % whereas it has been retained to 2.5 % in all the previous simulations.

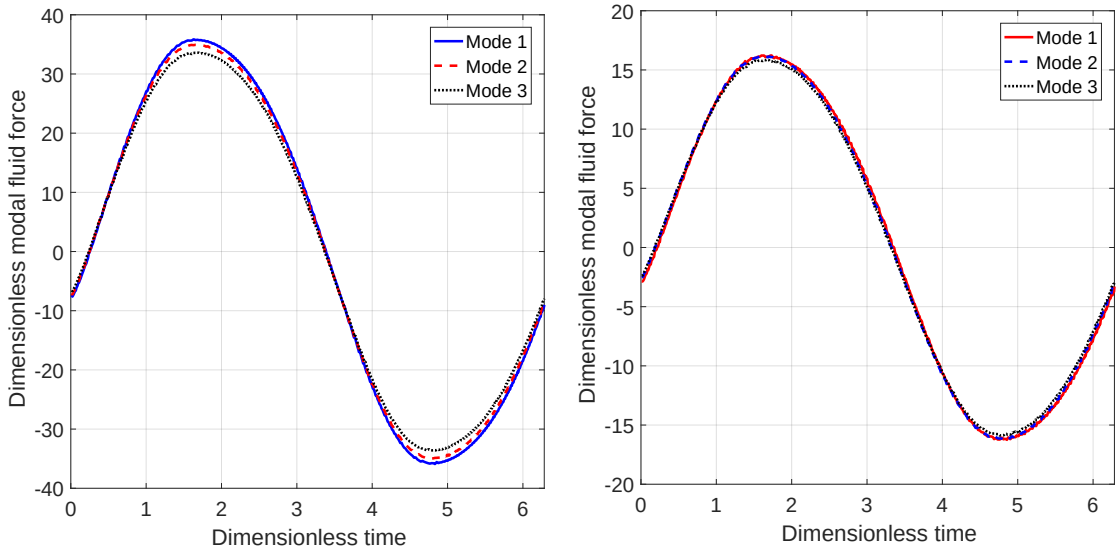

Figure 12: Time evolution of the dimensionless modal fluid force obtained numerically. Left: pinned-pinned case. Right: clamped-free case. This simulation has been performed to highlight the effect of the nonlinear convective term of the Navier-Stokes equations on the force signal. The Keulegan-Carpenter number is $KC = 2.5 \times 10^{-3}$ and the radius ratio $\varepsilon = 1.0375$, i.e. $KC/(\epsilon - 1) \approx 6.6$ %. The aspect ratio is $l = 35$.

Second, since the theory is based on the hypothesis of a narrow annulus, its predictions lose precision as the confinement is reduced, i.e. as ε increases. Indeed, as shown in Appendix H, the relative deviations given in Table H.13 (case $\varepsilon = 1.2$) are globally larger than those reported in Tables H.11 and H.12 (cases $\varepsilon = 1.0375$ and $\varepsilon = 1.1$, respectively).

Third, some relative deviations given in our tables of results, see Appendix G and Appendix H, are computed from small values of added-mass coefficients, especially for the off-diagonal terms (which in some cases are 100 or 1000 times smaller than the diagonal terms). Tiny differences between numerical and theoretical predictions on such small values automatically yield important relative deviations that should be considered with a critical eye.

Still, despite these identified causes of deviation, our theory satisfactorily reproduces the added-mass matrix (in particular the off-diagonal terms which cannot be obtained from the slender-body approximation), with a relative deviation that remains acceptable for all tested configurations.

8. Conclusion

We have considered the three-dimensional problem of two-coaxial finite length cylinders separated by a thin layer of fluid. We studied the case in which the inner cylinder is imposed a displacement corresponding to a bending mode of vibration of an Euler-Bernoulli beam. A new theoretical formulation based on the assumption of an elongated flexible cylinder, i.e., $l >> 1$, and a narrow fluid annulus has been carried out, leading to an explicit closed-form expression for the coefficients of the added-mass matrix. Our analytical formulation applies to any type of classical boundary conditions and can easily be implemented in any numerical computing environment.

We showed that the added-mass coefficient depends on the radius ratio of the configuration, acting like a confinement parameter, but also on the aspect ratio of the vibrating cylinder. The diagonal terms of the added-mass matrix are positive and always increase with the confinement and the aspect ratio. We also showed that the dry vibration modes generate off-diagonal terms (positive or negative) that vanish for a slender cylinder. The variations of these terms depend on both the boundary conditions and the wave-number of the vibration modes. The existence of these off-diagonal terms shows that for a cylinder of finite length, the fluid can modify the shape of the modes of vibration, leading to a non-zero modal coupling of the structural modes.

In addition to this new theoretical work and to assess the validity of its predictions, we performed numerical simulations with the open-source code TrioCFD. We carried out an in-depth comparison, considering different values of the aspect ratio ($l \geq 35$), radius ratio, and all classical types of boundary conditions. The numerical simulations successfully corroborated the theoretical predictions in all cases tested. In particular, the structure of the added-mass matrix (existence of off-diagonal terms, symmetry, anti-symmetry, sign of the coefficients) was perfectly recovered.

Finally, from a practical point of view, the presentation of our results in the form of dimensionless graphs and tables, covering all the classical types of boundary conditions, form complete charts for engineering applications. In addition to their academic interest, our results can easily be used in an industrial environment with fluid-structure interaction issues.

Having obtained a new formulation for the added-mass matrix, we are currently following the same approach to derive analytical expressions for the added-damping and stiffness matrices due to an axial flow. Then, we intend to carry out a stability analysis to establish the Argand's diagrams of all the boundary conditions tested in the present study. As a particular point of interest, we will focus on the effect of the off-diagonal terms generated by the finite length of the vibrating cylinder on the instability threshold.

Appendix A. List of the boundary conditions studied

In this appendix, we list in Table A.6 all the types of boundary conditions studied in the present article, providing the parameters associated with the dry vibration modes.

Boundary Conditions	$\chi^{(k)}$	Wavenumber equation	λ_j	σ	σ_j
Free – Free	$\begin{pmatrix} 1 \\ 1 \\ -\sigma \\ -\sigma \end{pmatrix}$	$\cosh(\lambda)\cos(\lambda) - 1 = 0$	$\begin{pmatrix} 4.7300 \\ 7.8532 \\ 10.996 \end{pmatrix}$	$\frac{\cosh(\lambda)-\cos(\lambda)}{\sinh(\lambda)-\sin(\lambda)}$	$\begin{pmatrix} 0.98250 \\ 1.0008 \\ 0.99997 \end{pmatrix}$
Clamped – Clamped	$\begin{pmatrix} 1 \\ -1 \\ -\sigma \\ \sigma \end{pmatrix}$	$\cosh(\lambda)\cos(\lambda) - 1 = 0$	$\begin{pmatrix} 4.7300 \\ 7.8532 \\ 10.996 \end{pmatrix}$	$\frac{\cosh(\lambda)-\cos(\lambda)}{\sinh(\lambda)-\sin(\lambda)}$	$\begin{pmatrix} 0.98250 \\ 1.0008 \\ 0.99997 \end{pmatrix}$
Free – Sliding	$\begin{pmatrix} 1 \\ 1 \\ -\sigma \\ -\sigma \end{pmatrix}$	$\tanh(\lambda) + \tan(\lambda) = 0$	$\begin{pmatrix} 2.3650 \\ 5.4978 \\ 8.6394 \end{pmatrix}$	$\frac{\sinh(\lambda)-\sin(\lambda)}{\cosh(\lambda)+\cos(\lambda)}$	$\begin{pmatrix} 0.98250 \\ 0.99997 \\ 1.0000 \end{pmatrix}$
Clamped – Sliding	$\begin{pmatrix} 1 \\ -1 \\ -\sigma \\ \sigma \end{pmatrix}$	$\tanh(\lambda) + \tan(\lambda) = 0$	$\begin{pmatrix} 2.3650 \\ 5.4978 \\ 8.6394 \end{pmatrix}$	$\frac{\sinh(\lambda)-\sin(\lambda)}{\cosh(\lambda)+\cos(\lambda)}$	$\begin{pmatrix} 0.98250 \\ 0.99997 \\ 1.0000 \end{pmatrix}$
Free – Pinned	$\begin{pmatrix} 1 \\ 1 \\ -\sigma \\ -\sigma \end{pmatrix}$	$\tan(\lambda) - \tanh(\lambda) = 0$	$\begin{pmatrix} 3.9266 \\ 7.0686 \\ 10.210 \end{pmatrix}$	$\frac{\cosh(\lambda)-\cos(\lambda)}{\sinh(\lambda)-\sin(\lambda)}$	$\begin{pmatrix} 1.0008 \\ 1.0000 \\ 1.0000 \end{pmatrix}$
Clamped – Pinned	$\begin{pmatrix} 1 \\ -1 \\ -\sigma \\ \sigma \end{pmatrix}$	$\tan(\lambda) - \tanh(\lambda) = 0$	$\begin{pmatrix} 3.9266 \\ 7.0686 \\ 10.210 \end{pmatrix}$	$\frac{\cosh(\lambda)-\cos(\lambda)}{\sinh(\lambda)-\sin(\lambda)}$	$\begin{pmatrix} 1.0008 \\ 1.0000 \\ 1.0000 \end{pmatrix}$
Clamped – Free	$\begin{pmatrix} 1 \\ -1 \\ -\sigma \\ \sigma \end{pmatrix}$	$\cosh(\lambda)\cos(\lambda) + 1 = 0$	$\begin{pmatrix} 1.8751 \\ 4.6941 \\ 7.8548 \end{pmatrix}$	$\frac{\cosh(\lambda)+\cos(\lambda)}{\sinh(\lambda)+\sin(\lambda)}$	$\begin{pmatrix} 0.73410 \\ 1.0185 \\ 0.99922 \end{pmatrix}$
Pinned – Pinned	$\begin{pmatrix} 0 \\ 0 \\ 0 \\ 1 \end{pmatrix}$	$\lambda_j = j\pi$	$\begin{pmatrix} \pi \\ 2\pi \\ 3\pi \end{pmatrix}$	X	X
Sliding – Pinned	$\begin{pmatrix} 0 \\ 1 \\ 0 \\ 0 \end{pmatrix}$	$\lambda_j = \frac{(2j-1)\pi}{2}$	$\begin{pmatrix} \pi/2 \\ 3\pi/2 \\ 5\pi/2 \end{pmatrix}$	X	X
Sliding – Sliding	$\begin{pmatrix} 0 \\ 1 \\ 0 \\ 0 \end{pmatrix}$	$\lambda_j = j\pi$	$\begin{pmatrix} \pi \\ 2\pi \\ 3\pi \end{pmatrix}$	X	X

Table A.6: Boundary conditions studied in the present work. The dry vibration modes are of the form $w_j(x) = \chi^{(1)}\cosh(\lambda_j x) + \chi^{(2)}\cos(\lambda_j x) + \chi_j^{(3)}\sinh(\lambda_j x) + \chi_j^{(4)}\sin(\lambda_j x)$, with $\chi^{(k)}$ given in the first column.

Appendix B. Analytical expressions for $m_{ij}^{(kq)}$ and $m_{nj}^{(q)}$

In this appendix we provide full analytical expressions for the terms $m_{ij}^{(kq)} = \left\langle w_i^{(k)}, w_j^{(q)} \right\rangle$ and $m_{nj}^{(q)}(l) = \left\langle \mathrm{e}^{(-1)^n lx}, w_j^{(q)}(x) \right\rangle$ appearing in equation (39).

The term $m_{ij}^{(kq)}$ corresponds to the projection of the $w_i^{(k)}$ mode onto the $w_j^{(q)}$ mode. As $w_i^{(k)}$ is a linear combination of sine and cosine functions,

$$w_i^{(k)}(x) = \chi^{(k)} \cos\left(\mathrm{i}^k \lambda_i x\right) + \chi_i^{(k+2)} (-\mathrm{i})^k \sin\left(\mathrm{i}^k \lambda_i x\right), \tag{B.1}$$

the term $m_{ij}^{(kq)}$ is a linear combination of the dot products

$$I_{c,ij}^{(kq)} = \left\langle \cos\left(\mathrm{i}^k \lambda_i x\right), \cos\left(\mathrm{i}^q \lambda_j x\right) \right\rangle, \tag{B.2a}$$

$$I_{ij}^{(kq)} = \left\langle \cos\left(\mathrm{i}^k \lambda_i x\right), \sin\left(\mathrm{i}^q \lambda_j x\right) \right\rangle, \tag{B.2b}$$

$$I_{s,ij}^{(kq)} = \left\langle \sin\left(\mathrm{i}^k \lambda_i x\right), \sin\left(\mathrm{i}^q \lambda_j x\right) \right\rangle. \tag{B.2c}$$

This linear combination writes

$$m_{ij}^{(kq)} = \chi^{(k)} \left[\chi^{(q)} I_{c,ij}^{(kq)} + \chi_j^{(q+2)} (-\mathrm{i})^q I_{ij}^{(kq)} \right] + \chi_i^{(k+2)} (-\mathrm{i})^k \left[\chi^{(q)} I_{ji}^{(qk)} + \chi_j^{(q+2)} (-\mathrm{i})^q I_{s,ij}^{(kq)} \right], \tag{B.3}$$

with

$$I_{c,ij}^{(kq)} = \begin{cases} \frac{1}{2} \frac{\left(\mathrm{i}^k \lambda_i + \cos\left(\mathrm{i}^k \lambda_i\right) \sin\left(\mathrm{i}^k \lambda_i\right)\right)(-i)^k}{\lambda_i} & \text{if} \quad (i=j) \cap (k=q) \\ \frac{\mathrm{i}^q \lambda_j \cos\left(\mathrm{i}^k \lambda_i\right) \sin(\mathrm{i}^q \lambda_j) - \mathrm{i}^k \lambda_i \sin\left(\mathrm{i}^k \lambda_i\right) \cos(\mathrm{i}^q \lambda_j)}{(-1)^q {\lambda_j}^2 - (-1)^k {\lambda_i}^2} & \text{otherwise} \end{cases}, \tag{B.4a}$$

$$I_{ij}^{(kq)} = \begin{cases} \frac{1}{2} \frac{\left(\sin\left(\mathrm{i}^k \lambda_i\right)\right)^2 (-i)^k}{\lambda_i} & \text{if} \quad (i=j) \cap (k=q) \\ \frac{-\mathrm{i}^q \lambda_j \cos\left(\mathrm{i}^k \lambda_i\right) \cos(\mathrm{i}^q \lambda_j) - \mathrm{i}^k \lambda_i \sin\left(\mathrm{i}^k \lambda_i\right) \sin(\mathrm{i}^q \lambda_j) + \mathrm{i}^q \lambda_j}{(-1)^q {\lambda_j}^2 - (-1)^k {\lambda_i}^2} & \text{otherwise} \end{cases}, \tag{B.4b}$$

$$I_{s,ij}^{(kq)} = \begin{cases} \frac{1}{2} \frac{\left(\mathrm{i}^k \lambda_i - \cos\left(\mathrm{i}^k \lambda_i\right) \sin\left(\mathrm{i}^k \lambda_i\right)\right)(-i)^k}{\lambda_i} & \text{if} \quad (i=j) \cap (k=q) \\ \frac{-\mathrm{i}^q \lambda_j \sin\left(\mathrm{i}^k \lambda_i\right) \cos(\mathrm{i}^q \lambda_j) + \mathrm{i}^k \lambda_i \cos\left(\mathrm{i}^k \lambda_i\right) \sin(\mathrm{i}^q \lambda_j)}{(-1)^q {\lambda_j}^2 - (-1)^k {\lambda_i}^2} & \text{otherwise} \end{cases}. \tag{B.4c}$$

The term $m_{nj}^{(q)}$ corresponds to the projection of the $\mathrm{e}^{(-1)^n lx}$ onto the $w_j^{(q)}$ mode. As $w_j^{(q)}$ is a linear combination of sine and cosine functions,

$$w_j^{(q)}(x) = \chi^{(q)} \cos\left(\mathrm{i}^q \lambda_j x\right) + \chi_j^{(q+2)} (-\mathrm{i})^q \sin\left(\mathrm{i}^q \lambda_j x\right), \tag{B.5}$$

the term $m_{nj}^{(q)}$ is a linear combination of the dot products

$$J_{c,nj}^{(q)}(l) = \left\langle \mathrm{e}^{(-1)^n lx}, \cos\left(\mathrm{i}^q \lambda_j x\right) \right\rangle, \tag{B.6a}$$

$$J_{s,nj}^{(q)}(l) = \left\langle \mathrm{e}^{(-1)^n lx}, \sin\left(\mathrm{i}^q \lambda_j x\right) \right\rangle. \tag{B.6b}$$

This linear combination writes

$$m_{nj}^{(q)} = \chi^{(q)} J_{c,nj}^{(q)} + \chi_j^{(q+2)} J_{s,nj}^{(q)}, \tag{B.7}$$

with

$$J_{c,nj}^{(q)}(l) = \begin{cases} \frac{\left(1 - \mathrm{e}^{-2l} + 2l\right)\delta_{1n} + \left(-1 + \mathrm{e}^{2l} + 2l\right)\delta_{2n}}{4l} & \text{if} \quad (\lambda_j = l) \cap (q=1) \\ \frac{\mathrm{e}^{l(-1)^n} \cos(\mathrm{i}^q \lambda_j)(-1)^n l + \mathrm{e}^{l(-1)^n} \mathrm{i}^q \sin(\mathrm{i}^q \lambda_j) \lambda_j - l(-1)^n}{l^2 + (-1)^q {\lambda_j}^2} & \text{otherwise} \end{cases}, \tag{B.8a}$$

$$J_{s,nj}^{(q)}(l) = \begin{cases} \mathrm{i} \frac{\left(2l - 1 + \mathrm{e}^{-2l}\right)\delta_{1n} + \left(\mathrm{e}^{2l} - 2l - 1\right)\delta_{2n}}{4l} & \text{if} \quad (\lambda_j = l) \cap (q=1) \\ \frac{-\mathrm{e}^{l(-1)^n} \mathrm{i}^q \cos(\mathrm{i}^q \lambda_j) \lambda_j + \mathrm{e}^{l(-1)^n} \sin(\mathrm{i}^q \lambda_j)(-1)^n l + \mathrm{i}^q \lambda_j}{l^2 + (-1)^q {\lambda_j}^2} & \text{otherwise} \end{cases}, \tag{B.8b}$$

with δ the Kronecker symbol.

The expressions (B.4) and (B.8), based on an index notation, can easily be implemented in any numeric computing environment. Reporting these expressions in equations (B.3), (B.7), (39) and eventually in equation (38) provides a straightforward and handful way to determine the modal added-mass matrix of a finite length cylinder vibrating in a confined environment, whatever the boundary conditions.

Appendix C. Added-mass for a rigid mode. Comparison to a reference

In this Appendix, we compare the predictions from our theory with the ones of [19], when the inner cylinder is imposed a rigid body motion. For such a particular case, the 3D potential fluid flow problem can be solved analytically, see [19], leading to a dimensionless added-mass coefficient

$$m_0^{(\mathrm{ref})}(l,\varepsilon) = \frac{l}{\pi}\frac{-\mathrm{K}_1^{'}\left(2\pi\varepsilon/l\right)\mathrm{I}_1\left(2\pi/l\right)+\mathrm{I}_1^{'}\left(2\pi\varepsilon/l\right)\mathrm{K}_1\left(2\pi/l\right)}{\mathrm{I}_1^{'}\left(2\pi/l\right)\mathrm{K}_1^{'}\left(2\pi\varepsilon/l\right)-\mathrm{I}_1^{'}\left(2\pi\varepsilon/l\right)\mathrm{K}_1^{'}\left(2\pi/l\right)}, \tag{C.1}$$

with K and I the modified Bessel functions. In our theory, the dimensionless added-mass coefficient for a rigid body motion is obtained by substituting $\lambda_i = 0$ in the equation (38), leading to

$$m_0(l,\varepsilon) = \frac{1}{\varepsilon-1}\left(1+2\frac{1-\cosh\left(l\right)}{l\sinh\left(l\right)}\right). \tag{C.2}$$

The two theories predict that the dimensionless added-mass coefficient for a rigid body motion increases with the aspect ratio, see Fig. C.13. From a physical point of view, it means that the frequency of oscillation of a rigid cylinder free to vibrate in a fluid at rest is all the greater as the cylinder is long. As expected, as $l \to \infty$ the two theories have asymptotic limits (41) and (21), which for a rigid body motion simplify to $m_0(l,\varepsilon) \to (\varepsilon-1)^{-1}$ and $m_0^{(\mathrm{ref})}(l,\varepsilon) \to (\varepsilon^2+1)(\varepsilon^2-1)^{-1}$. The ratio between these two limits is the same as $m_{ij}^{(\infty)}/m_{ij}^{(\mathrm{ref},\infty)}$, whose evolution was shown in Fig. 5. Here again, we conclude that our theory correctly predicts the added-mass of a cylinder imposed a rigid body motion, as long as the fluid layer remains sufficiently thin.

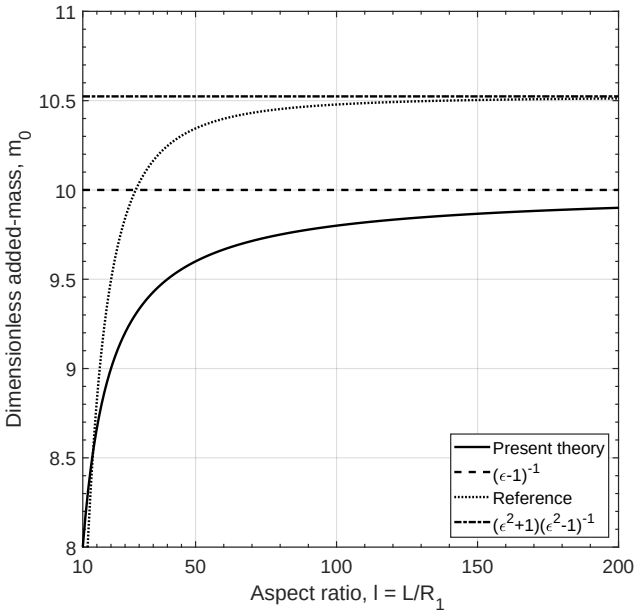

Figure C.13: Evolution of the dimensionless added-mass coefficient for a rigid body motion. The added-mass from the reference [19] is given by the equation (C.1). The added-mass from the present theory is given by the equation (C.2). The radius ratio is $\varepsilon = 1.1$.

Appendix D. Added-mass for a clamped-clamped mode. Comparison to a reference

In this Appendix, we compare the predictions from our theory with the ones of [18], when the inner cylinder is imposed a clamped-clamped vibration mode. For this particular case, [18] carried out a 3D potential fluid flow theory utilizing the assumption of a narrow annulus, leading to a dimensionless added-mass coefficient

$$m_{ij}^{(\mathrm{ref,CC})}(l,\varepsilon) = -\frac{1}{N_i N_j}\langle G_{1i}\psi_{1i} + G_{2i}\psi_{2i}, \psi_{1j} + \psi_{2j}\rangle, \tag{D.1}$$

with $\psi_{1i} = -\cos(\lambda_i x) + \sigma_i \sin(\lambda_i x)$, $\psi_{2i} = \cosh(\lambda_i x) - \sigma_i \sinh(\lambda_i x)$, N_i the infinite norm of the vibration mode $\psi_{1i} + \psi_{2i}$, and

$$G_{1i} = \frac{-q_i + \frac{1}{2}\tanh(q_i(\varepsilon-1))}{\left(q_i^2 - \frac{1}{4}\right)\tanh(q_i(\varepsilon-1))}, \qquad G_{2i} = \begin{vmatrix} \frac{c_i^* - \frac{1}{2}\tan(c_i^*(\varepsilon-1))}{\left(c_i^{*2}+\frac{1}{4}\right)\tan\left(c_i^*(\varepsilon-1)\right)} & \text{if} \quad \frac{\lambda_i}{l} > \frac{\sqrt{5}}{2} \\ \frac{-c_i + \frac{1}{2}\tanh(c_i(\varepsilon-1))}{\left(c_i{}^2-\frac{1}{4}\right)\tanh(c_i(\varepsilon-1))} & \text{if} \quad \frac{\lambda_i}{l} < \frac{\sqrt{5}}{2} \end{vmatrix}, \tag{D.2a}$$

$$q_i = \left[\frac{5}{4} + \left(\frac{\lambda_i}{l}\right)^2\right]^{1/2}, \qquad c_i^* = \left[\left(\frac{\lambda_i}{l}\right)^2 - \frac{5}{4}\right]^{1/2}, \quad c_i = \left[\frac{5}{4} - \left(\frac{\lambda_i}{l}\right)^2\right]^{1/2}. \tag{D.2b}$$

Clamped – **Clamped**	Present theory	Reference theory [18]	Relative deviation (%)
$l = 35$	$\begin{pmatrix} 3.926 & 0 & 0.03189 \\ 0 & 4.234 & 0 \\ 0.03222 & 0 & 4.024 \end{pmatrix}$	$\begin{pmatrix} 3.747 & 0 & 0.03150 \\ 0 & 4.043 & 0 \\ 0.03180 & 0 & 3.874 \end{pmatrix}$	4.78 1.32
$l = 70$	$\begin{pmatrix} 3.954 & 0 & 0.008200 \\ 0 & 4.349 & 0 \\ 0.008500 & 0 & 4.260 \end{pmatrix}$	$\begin{pmatrix} 3.774 & 0 & 0.007900 \\ 0 & 4.151 & 0 \\ 0.007900 & 0 & 4.090 \end{pmatrix}$	4.77 7.59
$l = 140$	$\begin{pmatrix} 3.962 & 0 & 0.002100 \\ 0 & 4.380 & 0 \\ 0.002400 & 0 & 4.325 \end{pmatrix}$	$\begin{pmatrix} 3.781 & 0 & 0.002000 \\ 0 & 4.179 & 0 \\ 0.002000 & 0 & 4.151 \end{pmatrix}$	4.80 20.0

Table D.7: Dimensionless added-mass matrix for the clamped-clamped case and three values of the aspect ratio $l = \{35, 70, 140\}$. The added-mass matrix from the present theory is given by the equation (38). The added-mass from the reference theory [18] is given by the equation (D.1). The radius ratio is $\varepsilon = 1.1$. The first (resp. second) number given in the last column of the table corresponds to the maximum relative deviation on the diagonal (resp. off-diagonal) terms.

In Table D.7, we compare the prediction of [18], given by (D.1), with our prediction, given by (38), considering three values of the aspect ratio, $l \in \{35, 70, 140\}$ and a radius ratio $\varepsilon = 1.1$.
The two theories are in excellent agreement regarding the diagonal terms, with a maximum relative deviation less than 5%. Both theories show that the diagonal terms depend on the wave-number of the vibration mode and slightly increase with the aspect ratio l. As we shall see later in Fig. 6, the diagonal coefficients for the clamped-clamped case actually quickly tend to their slender-body limits $\{3.964, 4.390, 4.346\}$ given in Table F.8. It follows that the increase of these coefficients for an aspect ratio varying from $l = 35$ to $l = 140$ remains quite limited.
Regarding the off-diagonal terms, the two theories predict that the only non-zero terms are m_{13} and m_{31}. These terms are shown to decrease with the aspect ratio of the cylinder, with an asymptotic limit equal to zero in the slender-body approximation, see also Fig. 6. The maximum relative deviation between the two theories is less than 8% for $l = 35$ and $l = 70$ and 20% for $l = 140$. Note that the 20% value has to be analysed with a critical eye as it is computed from very small terms (0.002400 and 0.002000) which, in addition, are a thousand times smaller than the diagonal terms.

Appendix E. Theoretical evolution of the added-mass coefficients with the aspect ratio

In this appendix, we show the theoretical evolution of the added-mass coefficients as a function of the aspect ratio, considering the boundary conditions which have not been presented in §6.1.

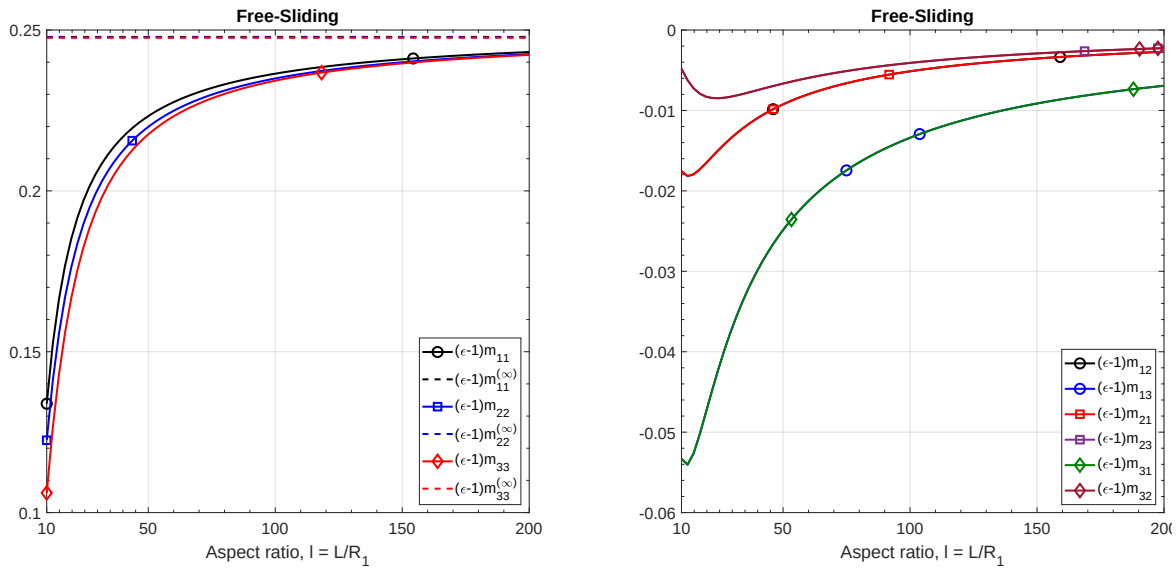

Figure E.14: Free-Sliding case. Evolution of the added-mass coefficient $(\varepsilon - 1)m_{ij}$, predicted by the equation (38), as a function of the aspect ratio l. Left : diagonal terms. The horizontal dashed lines correspond to the limit $l \to \infty$, given by the equation (41). Right : off-diagonal terms. These terms tend to 0 as $l \to \infty$. Symbols are used to distinguish superimposed curves.

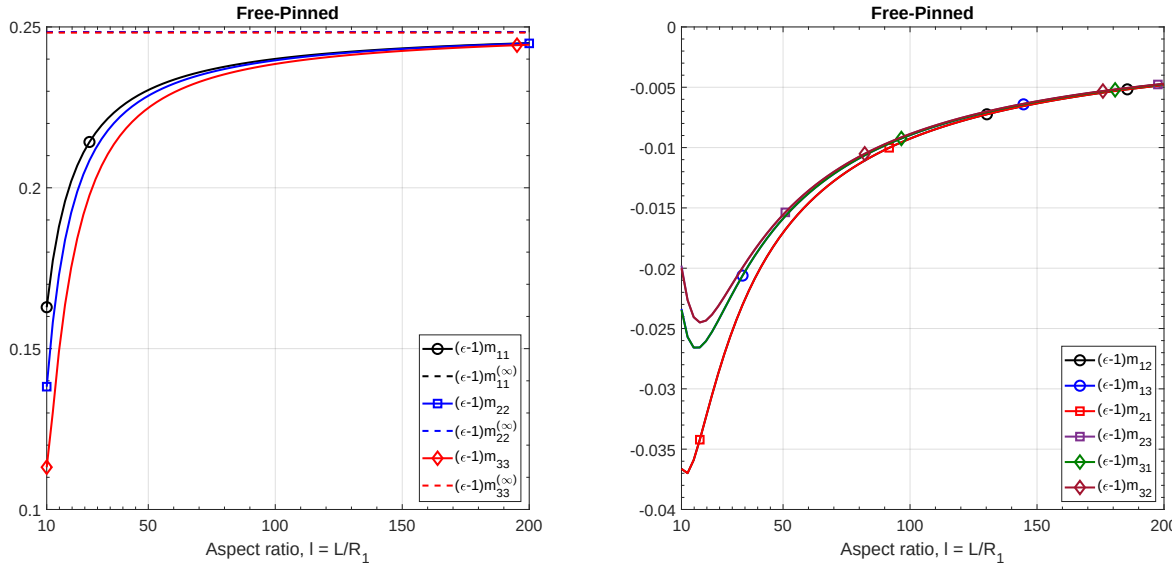

Figure E.15: Free-Pinned case. Evolution of the added-mass coefficient $(\varepsilon - 1)m_{ij}$, predicted by the equation (38), as a function of the aspect ratio l. Left : diagonal terms. The horizontal dashed lines correspond to the limit $l \to \infty$, given by the equation (41). Right : off-diagonal terms. These terms tend to 0 as $l \to \infty$. Symbols are used to distinguish superimposed curves.

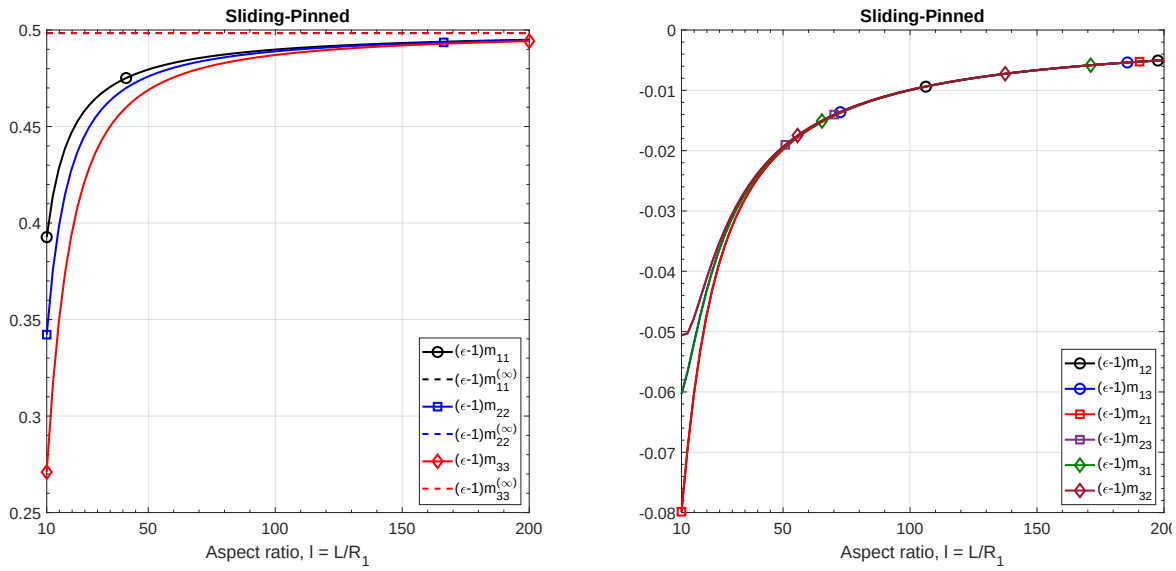

Figure E.16: Sliding-Pinned case. Evolution of the added-mass coefficient $(\varepsilon - 1)m_{ij}$, predicted by the equation (38), as a function of the aspect ratio l. Left : diagonal terms. The horizontal dashed lines correspond to the limit $l \to \infty$, given by the equation (41). Right : off-diagonal terms. These terms tend to 0 as $l \to \infty$. Symbols are used to distinguish superimposed curves.

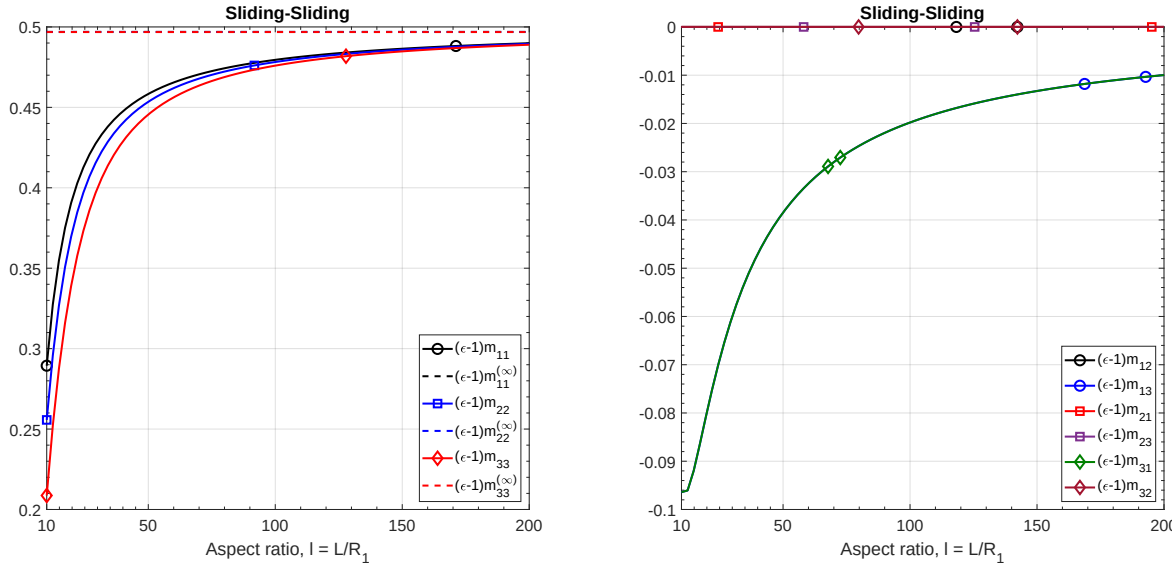

Figure E.17: Sliding-Sliding case. Evolution of the added-mass coefficient $(\varepsilon - 1)m_{ij}$, predicted by the equation (38), as a function of the aspect ratio l. Left : diagonal terms. The horizontal dashed lines correspond to the limit $l \to \infty$, given by the equation (41). Right : off-diagonal terms. These terms tend to 0 as $l \to \infty$. Symbols are used to distinguish superimposed curves.

Appendix F. Slender-body limit

In this appendix, we give the asymptotic limits $(\varepsilon - 1)\, m_{ij}^{(\infty)}$ corresponding to the added-mass matrix of an infinitely long cylinder, see equation (41).

Boundary Conditions	$(\varepsilon - 1)\, m_{ij}^{(\infty)}$
Free – Free	$\begin{pmatrix} 0.2469 & 0 & 0 \\ 0 & 0.2469 & 0 \\ 0 & 0 & 0.2456 \end{pmatrix}$
Clamped – Clamped	$\begin{pmatrix} 0.3964 & 0 & 0 \\ 0 & 0.4390 & 0 \\ 0 & 0 & 0.4346 \end{pmatrix}$
Free – Sliding	$\begin{pmatrix} 0.2479 & 0 & 0 \\ 0 & 0.2477 & 0 \\ 0 & 0 & 0.2476 \end{pmatrix}$
Clamped – Sliding	$\begin{pmatrix} 0.3949 & 0 & 0 \\ 0 & 0.4357 & 0 \\ 0 & 0 & 0.4358 \end{pmatrix}$
Free – Pinned	$\begin{pmatrix} 0.2484 & 0 & 0 \\ 0 & 0.2484 & 0 \\ 0 & 0 & 0.2482 \end{pmatrix}$
Clamped – Pinned	$\begin{pmatrix} 0.4390 & 0 & 0 \\ 0 & 0.4372 & 0 \\ 0 & 0 & 0.4367 \end{pmatrix}$
Clamped – Free	$\begin{pmatrix} 0.2485 & 0 & 0 \\ 0 & 0.2485 & 0 \\ 0 & 0 & 0.2485 \end{pmatrix}$
Pinned – Pinned	$\begin{pmatrix} 0.5000 & 0 & 0 \\ 0 & 0.5000 & 0 \\ 0 & 0 & 0.5000 \end{pmatrix}$
Sliding – Pinned	$\begin{pmatrix} 0.4984 & 0 & 0 \\ 0 & 0.4984 & 0 \\ 0 & 0 & 0.4984 \end{pmatrix}$
Sliding – Sliding	$\begin{pmatrix} 0.4969 & 0 & 0 \\ 0 & 0.4969 & 0 \\ 0 & 0 & 0.4969 \end{pmatrix}$

Table F.8: Dimensionless added-mass matrix of an infinitely long cylinder, given by the equation (41), for all the classical types of boundary conditions.

Appendix G. Effect of the aspect ratio

In this appendix we provide the theoretical and numerical predictions for the added-mass matrix, considering the ten types of boundary conditions listed in Table A.6, for $l \in \{70, 140\}$ and $\varepsilon = 1.1$.

Boundary Conditions	Present theory	Numerics TrioCFD	Relative deviation (%)
Rigid	9.714	10.62	8.53
Free – Free	$\begin{pmatrix} 2.227 & 0 & -0.2401 \\ 0 & 2.223 & 0 \\ -0.2400 & 0 & 2.196 \end{pmatrix}$	$\begin{pmatrix} 2.471 & 0 & -0.2288 \\ 0 & 2.461 & 0 \\ -0.2297 & 0 & 2.441 \end{pmatrix}$	10.0 4.94
Clamped – Clamped	$\begin{pmatrix} 3.954 & 0 & 0.008200 \\ 0 & 4.349 & 0 \\ 0.008500 & 0 & 4.260 \end{pmatrix}$	$\begin{pmatrix} 4.309 & 0 & 0.008700 \\ 0 & 4.738 & 0 \\ 0.01012 & 0 & 4.661 \end{pmatrix}$	8.60 16.0
Free – Sliding	$\begin{pmatrix} 2.307 & -0.07010 & -0.1855 \\ -0.07010 & 2.285 & -0.05360 \\ -0.1856 & -0.05360 & 2.272 \end{pmatrix}$	$\begin{pmatrix} 2.551 & -0.06660 & -0.1755 \\ -0.06700 & 2.525 & -0.05210 \\ -0.1763 & -0.05230 & 2.508 \end{pmatrix}$	9.56 5.70
Clamped – Sliding	$\begin{pmatrix} 3.819 & 0.1339 & -0.1299 \\ 0.1339 & 4.227 & 0.1270 \\ -0.1299 & 0.1270 & 4.192 \end{pmatrix}$	$\begin{pmatrix} 4.201 & 0.1260 & -0.1225 \\ 0.1275 & 4.642 & 0.1217 \\ -0.1225 & 0.1219 & 4.601 \end{pmatrix}$	9.09 6.27
Free – Pinned	$\begin{pmatrix} 2.359 & -0.1278 & -0.1218 \\ -0.1278 & 2.350 & -0.1201 \\ -0.1218 & -0.1201 & 2.329 \end{pmatrix}$	$\begin{pmatrix} 2.598 & -0.1220 & -0.1158 \\ -0.1223 & 2.585 & -0.1156 \\ -0.1161 & -0.1158 & 2.560 \end{pmatrix}$	9.20 5.18
Clamped – Pinned	$\begin{pmatrix} 4.380 & 0 & 0 \\ 0 & 4.334 & 0.0070 \\ 0 & 0.0070 & 4.286 \end{pmatrix}$	$\begin{pmatrix} 4.774 & 0 & 0 \\ 0 & 4.719 & 0.0079 \\ 0 & 0.0079 & 4.668 \end{pmatrix}$	8.25 11.3
Clamped – Free	$\begin{pmatrix} 2.360 & 0.1341 & -0.1261 \\ 0.1341 & 2.360 & 0.1285 \\ -0.1261 & 0.1285 & 2.350 \end{pmatrix}$	$\begin{pmatrix} 2.603 & 0.1267 & -0.1191 \\ 0.1278 & 2.598 & 0.1238 \\ -0.1199 & 0.1243 & 2.584 \end{pmatrix}$	9.33 5.88
Pinned – Pinned	$\begin{pmatrix} 4.990 & 0 & 0 \\ 0 & 4.960 & 0 \\ 0 & 0 & 4.911 \end{pmatrix}$	$\begin{pmatrix} 5.461 & 0 & 0 \\ 0 & 5.426 & 0 \\ 0 & 0 & 5.368 \end{pmatrix}$	8.62 X
Sliding – Pinned	$\begin{pmatrix} 4.855 & -0.1421 & -0.1410 \\ -0.1421 & 4.836 & -0.1404 \\ -0.1410 & -0.1404 & 4.798 \end{pmatrix}$	$\begin{pmatrix} 5.335 & -0.1332 & -0.1336 \\ -0.1347 & 5.312 & -0.1335 \\ -0.1335 & -0.1335 & 5.267 \end{pmatrix}$	9.00 6.68
Sliding – Sliding	$\begin{pmatrix} 4.705 & 0 & -0.2801 \\ 0 & 4.679 & 0 \\ -0.2801 & 0 & 4.635 \end{pmatrix}$	$\begin{pmatrix} 5.191 & 0 & -0.2638 \\ 0 & 5.158 & 0 \\ -0.2653 & 0 & 5.106 \end{pmatrix}$	9.36 6.18

Table G.9: Dimensionless added-mass matrix for all the classical types of boundary conditions. The added-mass from the present theory is given by the equation (38). The aspect ratio is $l = 70$ and the radius ratio is $\varepsilon = 1.1$. The first (resp. second) number given in the last column of the table corresponds to the maximum relative deviation on the diagonal (resp. off-diagonal) terms.

Boundary Conditions	Present theory	Numerics TrioCFD	Relative deviation (%)
Rigid	9.857	10.77	8.47
Free – Free	$\begin{pmatrix} 2.360 & 0 & -0.1314 \\ 0 & 2.359 & 0 \\ -0.1313 & 0 & 2.342 \end{pmatrix}$	$\begin{pmatrix} 2.614 & 0 & -0.1252 \\ 0 & 2.612 & 0 \\ -0.1256 & 0 & 2.606 \end{pmatrix}$	10.1 4.95
Clamped – Clamped	$\begin{pmatrix} 3.962 & 0 & 0.002100 \\ 0 & 4.380 & 0 \\ 0.0024 & 0 & 4.325 \end{pmatrix}$	$\begin{pmatrix} 4.329 & 0 & 0.0020 \\ 0 & 4.783 & 0 \\ 0.0025 & 0 & 4.743 \end{pmatrix}$	8.81 4.99
Free – Sliding	$\begin{pmatrix} 2.403 & -0.03770 & -0.09760 \\ -0.03770 & 2.393 & -0.03090 \\ -0.09760 & -0.03090 & 2.389 \end{pmatrix}$	$\begin{pmatrix} 2.657 & -0.03560 & -0.09240 \\ -0.03590 & 2.645 & -0.02970 \\ -0.09290 & -0.02980 & 2.640 \end{pmatrix}$	9.56 5.90
Clamped – Sliding	$\begin{pmatrix} 3.892 & 0.06680 & -0.06610 \\ 0.06680 & 4.304 & 0.06310 \\ -0.06610 & 0.06310 & 4.295 \end{pmatrix}$	$\begin{pmatrix} 4.293 & 0.06250 & -0.06280 \\ 0.06390 & 4.743 & 0.06060 \\ -0.06280 & 0.06070 & 4.733 \end{pmatrix}$	9.34 6.88
Free – Pinned	$\begin{pmatrix} 2.429 & -0.06770 & -0.06610 \\ -0.06770 & 2.426 & -0.06570 \\ -0.06610 & -0.06560 & 2.420 \end{pmatrix}$	$\begin{pmatrix} 2.681 & -0.06440 & -0.06310 \\ -0.06460 & 2.677 & -0.06290 \\ -0.06320 & -0.06290 & 2.671 \end{pmatrix}$	9.40 5.12
Clamped – Pinned	$\begin{pmatrix} 4.387 & 0 & 0 \\ 0 & 4.363 & 0.001800 \\ 0 & 0.001800 & 4.347 \end{pmatrix}$	$\begin{pmatrix} 4.828 & 0 & 0 \\ 0 & 4.798 & 0.002154 \\ 0 & 0.002154 & 4.785 \end{pmatrix}$	9.15 16.4
Clamped – Free	$\begin{pmatrix} 2.429 & 0.06920 & -0.06720 \\ 0.06920 & 2.429 & 0.06780 \\ -0.06720 & 0.06780 & 2.427 \end{pmatrix}$	$\begin{pmatrix} 2.682 & 0.06520 & -0.06380 \\ 0.06590 & 2.681 & 0.06500 \\ -0.06390 & 0.06520 & 2.677 \end{pmatrix}$	10.2 5.70
Pinned – Pinned	$\begin{pmatrix} 4.997 & 0 & 0 \\ 0 & 4.990 & 0 \\ 0 & 0 & 4.977 \end{pmatrix}$	$\begin{pmatrix} 5.498 & 0 & 0 \\ 0 & 5.489 & 0 \\ 0 & 0 & 5.474 \end{pmatrix}$	9.11 X
Sliding – Pinned	$\begin{pmatrix} 4.928 & -0.07130 & -0.07120 \\ -0.07130 & 4.923 & -0.07110 \\ -0.07120 & -0.07110 & 4.913 \end{pmatrix}$	$\begin{pmatrix} 5.432 & -0.06630 & -0.06800 \\ -0.06780 & 5.427 & -0.06770 \\ -0.06780 & -0.06770 & 5.414 \end{pmatrix}$	9.29 7.54
Sliding – Sliding	$\begin{pmatrix} 4.855 & 0 & -0.1421 \\ 0 & 4.848 & 0 \\ -0.1421 & 0 & 4.836 \end{pmatrix}$	$\begin{pmatrix} 5.361 & 0 & -0.1339 \\ 0 & 5.353 & 0 \\ -0.1354 & 0 & 5.339 \end{pmatrix}$	9.44 6.12

Table G.10: Dimensionless added-mass matrix for all the classical types of boundary conditions. The added-mass from the present theory is given by the equation (38). The aspect ratio is $l = 140$ and the radius ratio is $\varepsilon = 1.1$. The first (resp. second) number given in the last column of the table corresponds to the maximum relative deviation on the diagonal (resp. off-diagonal) terms.

Appendix H. Effect of the radius ratio

In this appendix we provide the theoretical and numerical predictions for the added-mass matrix, considering the ten types of boundary conditions listed in Table A.6, for $l = 35$ and $\varepsilon \in \{1.0375, 1.1, 1.2\}$.

Boundary Conditions	Present theory	Numerics TrioCFD	Relative deviation (%)
Rigid	25.14	27.05	7.06
Free – Free	$\begin{pmatrix} 5.279 & 0 & -1.046 \\ 0 & 5.244 & 0 \\ -1.046 & 0 & 5.083 \end{pmatrix}$	$\begin{pmatrix} 5.855 & 0 & -1.066 \\ 0 & 5.780 & 0 \\ -1.021 & 0 & 5.383 \end{pmatrix}$	9.84 2.45
Clamped – Clamped	$\begin{pmatrix} 10.47 & 0 & 0.08500 \\ 0 & 11.29 & 0 \\ 0.08590 & 0 & 10.73 \end{pmatrix}$	$\begin{pmatrix} 11.63 & 0 & 0.09078 \\ 0 & 12.06 & 0 \\ 0.09231 & 0 & 11.44 \end{pmatrix}$	9.97 6.94
Free – Sliding	$\begin{pmatrix} 5.660 & -0.3206 & -0.8819 \\ -0.3206 & 5.527 & -0.2102 \\ -0.8819 & -0.2102 & 5.413 \end{pmatrix}$	$\begin{pmatrix} 6.258 & -0.3290 & -0.8970 \\ -0.3284 & 6.103 & -0.2196 \\ -0.8580 & -0.2114 & 5.723 \end{pmatrix}$	9.55 2.78
Clamped – Sliding	$\begin{pmatrix} 9.788 & 0.7105 & -0.6524 \\ 0.7105 & 10.80 & 0.6656 \\ -0.6524 & 0.6656 & 10.47 \end{pmatrix}$	$\begin{pmatrix} 10.55 & 0.7223 & -0.6404 \\ 0.6969 & 11.51 & 0.6573 \\ -0.6374 & 0.6567 & 11.15 \end{pmatrix}$	7.22 2.35
Free – Pinned	$\begin{pmatrix} 5.927 & -0.6019 & -0.5406 \\ -0.6019 & 5.833 & -0.5239 \\ -0.5406 & -0.5238 & 5.646 \end{pmatrix}$	$\begin{pmatrix} 6.318 & -0.5955 & -0.5301 \\ -0.5916 & 6.164 & -0.5180 \\ -0.5278 & -0.5175 & 5.938 \end{pmatrix}$	6.18 2.42
Clamped – Pinned	$\begin{pmatrix} 11.60 & 0.0403 & 0.0352 \\ 0.0403 & 11.27 & 0.0715 \\ 0.0352 & 0.0715 & 10.82 \end{pmatrix}$	$\begin{pmatrix} 12.40 & 0.04434 & 0.03738 \\ 0.04060 & 11.95 & 0.07414 \\ 0.03968 & 0.07270 & 11.39 \end{pmatrix}$	6.45 11.3
Clamped – Free	$\begin{pmatrix} 5.939 & 0.6682 & -0.5841 \\ 0.6682 & 5.937 & 0.6098 \\ -0.5841 & 0.6098 & 5.838 \end{pmatrix}$	$\begin{pmatrix} 6.370 & 0.6695 & -0.5732 \\ 0.6576 & 6.324 & 0.6063 \\ -0.5724 & 0.6034 & 6.185 \end{pmatrix}$	6.11 3.20
Pinned – Pinned	$\begin{pmatrix} 13.23 & 0 & 0 \\ 0 & 12.92 & 0 \\ 0 & 0 & 12.43 \end{pmatrix}$	$\begin{pmatrix} 14.12 & 0 & 0 \\ 0 & 13.86 & 0 \\ 0 & 0 & 13.17 \end{pmatrix}$	6.78 X
Sliding – Pinned	$\begin{pmatrix} 12.55 & -0.7468 & -0.7239 \\ -0.7468 & 12.36 & -0.7125 \\ -0.7239 & -0.7125 & 12.00 \end{pmatrix}$	$\begin{pmatrix} 13.38 & -0.7516 & -0.7025 \\ -0.7316 & 13.18 & -0.6987 \\ -0.7110 & -0.7022 & 12.84 \end{pmatrix}$	6.54 3.04
Sliding – Sliding	$\begin{pmatrix} 11.73 & 0 & -1.409 \\ 0 & 11.49 & 0 \\ -1.409 & 0 & 11.11 \end{pmatrix}$	$\begin{pmatrix} 12.64 & 0 & -1.403 \\ 0 & 12.64 & 0 \\ -1.418 & 0 & 12.20 \end{pmatrix}$	9.09 0.630

Table H.11: Dimensionless added-mass matrix for all the classical types of boundary conditions. The added-mass from the present theory is given by the equation (38). The aspect ratio is $l = 35$ and the radius ratio is $\varepsilon = 1.0375$. The first (resp. second) number given in the last column of the table corresponds to the maximum relative deviation on the diagonal (resp. off-diagonal) terms.

Boundary Conditions	Present theory	Numerics TrioCFD	Relative deviation (%)
Rigid	9.429	10.31	8.54
Free – Free	$\begin{pmatrix} 1.980 & 0 & -0.3922 \\ 0 & 1.966 & 0 \\ -0.3921 & 0 & 1.906 \end{pmatrix}$	$\begin{pmatrix} 2.223 & 0 & -0.3761 \\ 0 & 2.189 & 0 \\ -0.3753 & 0 & 2.010 \end{pmatrix}$	10.9 4.47
Clamped – Clamped	$\begin{pmatrix} 3.926 & 0 & 0.03189 \\ 0 & 4.234 & 0 \\ 0.03222 & 0 & 4.024 \end{pmatrix}$	$\begin{pmatrix} 4.274 & 0 & 0.0369 \\ 0 & 4.598 & 0 \\ 0.0382 & 0 & 4.381 \end{pmatrix}$	8.14 15.7
Free – Sliding	$\begin{pmatrix} 2.122 & -0.1202 & -0.3307 \\ -0.1202 & 2.073 & -0.07882 \\ -0.3307 & -0.07882 & 2.030 \end{pmatrix}$	$\begin{pmatrix} 2.370 & -0.1157 & -0.3135 \\ -0.1167 & 2.310 & -0.0793 \\ -0.3154 & -0.0800 & 2.250 \end{pmatrix}$	10.5 5.49
Clamped – Sliding	$\begin{pmatrix} 3.671 & 0.2664 & -0.2446 \\ 0.2664 & 4.050 & 0.2496 \\ -0.2446 & 0.2496 & 3.928 \end{pmatrix}$	$\begin{pmatrix} 4.059 & 0.2538 & -0.2300 \\ 0.2555 & 4.461 & 0.2414 \\ -0.2299 & 0.2415 & 4.3135 \end{pmatrix}$	9.56 6.81
Free – Pinned	$\begin{pmatrix} 2.223 & -0.2257 & -0.2027 \\ -0.2257 & 2.188 & -0.1965 \\ -0.2027 & -0.1964 & 2.117 \end{pmatrix}$	$\begin{pmatrix} 2.461 & -0.2179 & -0.1931 \\ -0.2187 & 2.411 & -0.1925 \\ -0.1945 & -0.1932 & 2.323 \end{pmatrix}$	9.67 4.97
Clamped – Pinned	$\begin{pmatrix} 4.349 & 0.01511 & 0.01321 \\ 0.01511 & 4.226 & 0.02682 \\ 0.01318 & 0.02683 & 4.059 \end{pmatrix}$	$\begin{pmatrix} 4.736 & 0.01660 & 0.01630 \\ 0.01710 & 4.592 & 0.02920 \\ 0.01706 & 0.02900 & 4.297 \end{pmatrix}$	8.17 22.7
Clamped – Free	$\begin{pmatrix} 2.227 & 0.2506 & -0.2190 \\ 0.2506 & 2.227 & 0.2287 \\ -0.2190 & 0.2287 & 2.189 \end{pmatrix}$	$\begin{pmatrix} 2.475 & 0.2391 & -0.2067 \\ 0.2405 & 2.463 & 0.2232 \\ -0.2081 & 0.2241 & 2.410 \end{pmatrix}$	10.0 5.95
Pinned – Pinned	$\begin{pmatrix} 4.960 & 0 & 0 \\ 0 & 4.844 & 0 \\ 0 & 0 & 4.662 \end{pmatrix}$	$\begin{pmatrix} 5.430 & 0 & 0 \\ 0 & 5.294 & 0 \\ 0 & 0 & 5.081 \end{pmatrix}$	8.60 X
Sliding – Pinned	$\begin{pmatrix} 4.705 & -0.2801 & -0.2715 \\ -0.2801 & 4.635 & -0.2672 \\ -0.2715 & -0.2672 & 4.501 \end{pmatrix}$	$\begin{pmatrix} 5.191 & -0.2650 & -0.2570 \\ -0.2668 & 5.107 & -0.2548 \\ -0.2567 & -0.2547 & 4.946 \end{pmatrix}$	9.36 5.76
Sliding – Sliding	$\begin{pmatrix} 4.398 & 0 & -0.5285 \\ 0 & 4.308 & 0 \\ -0.5285 & 0 & 4.165 \end{pmatrix}$	$\begin{pmatrix} 4.891 & 0 & -0.4981 \\ 0 & 4.779 & 0 \\ -0.4996 & 0 & 4.602 \end{pmatrix}$	10.1 6.10

Table H.12: Dimensionless added-mass matrix for all the classical types of boundary conditions. The added-mass from the present theory is given by the equation (38). The aspect ratio is $l = 35$ and the radius ratio is $\varepsilon = 1.1$. The first (resp. second) number given in the last column of the table corresponds to the maximum relative deviation on the diagonal (resp. off-diagonal) terms.

Boundary Conditions	Present theory	Numerics TrioCFD	Relative deviation (%)
Rigid	4.714	5.320	11.4
Free – Free	$\begin{pmatrix} 0.9898 & 0 & -0.1961 \\ 0 & 0.9832 & 0 \\ -0.1961 & 0 & 0.9531 \end{pmatrix}$	$\begin{pmatrix} 1.151 & 0 & -0.1824 \\ 0 & 1.128 & 0 \\ -0.1830 & 0 & 1.077 \end{pmatrix}$	12.9 7.15
Clamped – Clamped	$\begin{pmatrix} 1.963 & 0 & 0.01590 \\ 0 & 2.117 & 0 \\ 0.01610 & 0 & 2.012 \end{pmatrix}$	$\begin{pmatrix} 2.197 & 0 & 0.02095 \\ 0 & 2.373 & 0 \\ 0.02130 & 0 & 2.233 \end{pmatrix}$	10.8 24.4
Free – Sliding	$\begin{pmatrix} 1.061 & -0.06010 & -0.1654 \\ -0.06010 & 1.036 & -0.03940 \\ -0.1654 & -0.03940 & 1.015 \end{pmatrix}$	$\begin{pmatrix} 1.234 & -0.05683 & -0.1524 \\ -0.05748 & 1.200 & -0.03974 \\ -0.1537 & -0.04031 & 1.164 \end{pmatrix}$	14.0 8.53
Clamped – Sliding	$\begin{pmatrix} 1.835 & 0.1332 & -0.1223 \\ 0.1332 & 2.025 & 0.1248 \\ -0.1223 & 0.1248 & 1.964 \end{pmatrix}$	$\begin{pmatrix} 2.104 & 0.1244 & -0.1110 \\ 0.1251 & 2.307 & 0.1189 \\ -0.1111 & 0.1190 & 2.225 \end{pmatrix}$	12.1 10.1
Free – Pinned	$\begin{pmatrix} 1.111 & -0.1129 & -0.1014 \\ -0.1129 & 1.094 & -0.09820 \\ -0.1014 & -0.09820 & 1.059 \end{pmatrix}$	$\begin{pmatrix} 1.276 & -0.1071 & -0.09385 \\ -0.1077 & 1.246 & -0.09524 \\ -0.09492 & -0.09581 & 1.196 \end{pmatrix}$	12.9 8.04
Clamped – Pinned	$\begin{pmatrix} 2.175 & 0 & 0 \\ 0 & 2.113 & 0.01340 \\ 0 & 0.01340 & 2.029 \end{pmatrix}$	$\begin{pmatrix} 2.449 & 0 & 0 \\ 0 & 2.370 & 0.01573 \\ 0 & 0.01573 & 2.264 \end{pmatrix}$	11.2 14.8
Clamped – Free	$\begin{pmatrix} 1.114 & 0.1253 & -0.1095 \\ 0.1253 & 1.113 & 0.1143 \\ -0.1095 & 0.1143 & 1.095 \end{pmatrix}$	$\begin{pmatrix} 1.278 & 0.1164 & -0.09944 \\ 0.1172 & 1.269 & 0.1098 \\ -0.1007 & 0.1112 & 1.239 \end{pmatrix}$	12.8 8.73
Pinned – Pinned	$\begin{pmatrix} 2.480 & 0 & 0 \\ 0 & 2.422 & 0 \\ 0 & 0 & 2.331 \end{pmatrix}$	$\begin{pmatrix} 2.779 & 0 & 0 \\ 0 & 2.708 & 0 \\ 0 & 0 & 2.587 \end{pmatrix}$	10.7 X
Sliding – Pinned	$\begin{pmatrix} 2.353 & -0.1400 & -0.1357 \\ -0.1400 & 2.318 & -0.1336 \\ -0.1357 & -0.1336 & 2.251 \end{pmatrix}$	$\begin{pmatrix} 2.690 & -0.1294 & -0.1246 \\ -0.1301 & 2.642 & -0.1243 \\ -0.1245 & -0.1243 & 2.553 \end{pmatrix}$	12.5 8.99
Sliding – Sliding	$\begin{pmatrix} 2.199 & 0 & -0.2643 \\ 0 & 2.154 & 0 \\ -0.2643 & 0 & 2.083 \end{pmatrix}$	$\begin{pmatrix} 2.541 & 0 & -0.2415 \\ 0 & 2.477 & 0 \\ -0.2422 & 0 & 2.379 \end{pmatrix}$	13.4 9.44

Table H.13: Dimensionless added-mass matrix for all the classical types of boundary conditions. The added-mass from the present theory is given by the equation (38). The aspect ratio is $l = 35$ and the radius ratio is $\varepsilon = 1.2$. The first (resp. second) number given in the last column of the table corresponds to the maximum relative deviation on the diagonal (resp. off-diagonal) terms.

References

[1] Y. Bergamaschi, Y. Bouilloux, P. Chantoin, B. Guigon, X. Bravo, C. Germain, M. Rommens, P. Tremodeux, Jules horowitz reactor, basic design, in: Proc. of ENC, 2002.

[2] R. D. Blevins, Flow-induced vibration, 2nd Edition, Krieger Publishing Company, 1990.

[3] S. S. Chen, M. W. Wambsganss, Parallel-flow-induced vibration of fuel rods, Nuclear Engineering and Design 18 (2) (1972) 253–278.

[4] S. S. Chen, M. W. Wambsganss, J. A. Jendrzejczyk, Added mass and damping of a vibrating rod in confined viscous fluids, Journal of Applied Mechanics. 43 (1976) 325–329.

[5] M. P. Paidoussis, Dynamics of cylindrical structures subjected to axial flow, Journal of Sound and Vibration 29 (1973) 365–385.

[6] S. S. Chen, Dynamics of heat exchanger tube banks, Journal of Fluids Engineering. 99 (1977) 462–469.

[7] R. Lagrange, X. Delaune, P. Piteau, L. Borsoi, J. Antunes, A new analytical approach for modeling the added mass and hydrodynamic interaction of two cylinders subjected to large motions in a potential stagnant fluid, Journal of Fluids and Structures. 77 (2018) 102–114.

[8] R. Lagrange, Y. Fraigneau, New estimations of the added mass and damping of two cylinders vibrating in a viscous fluid, from theoretical and numerical approaches, Journal of Fluids and Structures. 92 (2020) 102818.

[9] D. Panunzio, M. A. Puscas, R. Lagrange, FSI-Vibrations of immersed cylinders. Simulations with the engineering open-source code TrioCFD. Test cases and experimental comparisons, arXiv 2101.11322.

[10] R. J. Fritz, The Effect of Liquids on the Dynamic Motions of Immersed Solids, Journal of Engineering for Industry 94 (1) (1972) 167–173.

[11] M. P. Paidoussis, S. J. Price, E. de Langre, Fluid-Structure Interactions: Cross-Flow-Induced Instabilities, Cambridge University Press, 2010.

[12] M. P. Paidoussis, Fluid-structure interactions : slender structures and axial flow. Volume 1, 2nd Edition, Elsevier, London, 2014.

[13] M. P. Paidoussis, Fluid-structure interactions. Volume 2 : slender structures and axial flow, 2nd Edition, Academic Press, London, England, 2016.

[14] S. S. Chen, Flow-induced vibration of circular cylindrical structures, Hemisphere Pub. Corp, 1987.

[15] F. Axisa, J. Antunes, Modelling of Mechanical Systems: Fluid-structure Interaction, Butterworth-Heinemann Ltd, 2006.

[16] M. Paidoussis, M.Ostoja-Starzewski, Dynamics of a flexible cylinder in subsonic axial flow, AIAA Journal.

[17] D. Mateescu, M. P. Paidoussis, Annular-flow-induced vibrations of an axially variable body of revolution in a duct of variable crosssection, in: Proceedings of the ASME Symposium on Flow-Induced Vibrations, Vol. 4, 1984, pp. 53–69.

[18] M. P. Paidoussis, D. Mateescu, W.-G. Sim, Dynamics and Stability of a Flexible Cylinder in a Narrow Coaxial Cylindrical Duct Subjected to Annular Flow, Journal of Applied Mechanics 57 (1) (1990) 232–240.

[19] S. S. Chen, H. Chung, Design guide for calculating hydrodynamic mass. part i: circular cylindrical structures, Argonne National Laboratory technical report ANL-CT-76-45.

[20] P. E. Angeli, M. A. Puscas, G. Fauchet, A. Cartalade, FVCA8 benchmark for the Stokes and Navier-Stokes equations with the TrioCFD code – benchmark session, in: Finite Volumes for Complex Applications VIII - Methods and Theoretical Aspects., 2017, pp. 181–202.

[21] C. Fiorini, B. Després, M. A. Puscas, Sensitivity equation method for the navier-stokes equations applied to uncertainty propagation, International Journal for Numerical Methods in Fluids. (2020) 1–23.